Dark Energy Survey: Implications for cosmological expansion models from the final DES baryon acoustic oscillation and supernova data

T. M. C. Abbott,[1] M. Acevedo,[2] M. Adamow,[3] M. Aguena,[4] A. Alarcon,[5] S. Allam,[6] O. Alves,[7] F. Andrade-Oliveira,[8] J. Annis,[6] P. Armstrong,[9] S. Avila,[10] D. Bacon,[11] K. Bechtol,[12] J. Blazek,[13] S. Bocquet,[14] D. Brooks,[15] D. Brout,[16] D. L. Burke,[17,18] H. Camacho,[19,20,4] R. Camilleri,[21] G. Campailla,[22] A. Carnero Rosell,[23,4,24] A. Carr,[25] J. Carretero,[26] F. J. Castander,[27,5] R. Cawthon,[28] K. C. Chan,[29,30] C. Chang,[31,32] R. Chen,[2] C. Conselice,[33,34] M. Costanzi,[35,36,37] M. Crocce,[27,5] L. N. da Costa,[4] M. E. S. Pereira,[38] T. M. Davis,[21] J. De Vicente,[10] N. Deiosso,[10] S. Desai,[39] H. T. Diehl,[6] S. Dodelson,[31,6,32] P. Doel,[15] C. Doux,[40,41] A. Drlica-Wagner,[31,6,32] J. Elvin-Poole,[42] S. Everett,[43] I. Ferrero,[44] A. Ferté,[18] B. Flaugher,[6] P. Fosalba,[27,5] J. Frieman,[31,6,32] L. Galbany,[27,5] J. García-Bellido,[45] M. Gatti,[40,32] E. Gaztanaga,[27,11,5] G. Giannini,[26,32] D. Gruen,[14] R. A. Gruendl,[3,46] G. Gutierrez,[6] W. G. Hartley,[47] K. Herner,[6] S. R. Hinton,[21] D. L. Hollowood,[48] K. Honscheid,[49,50] D. Huterer,[7] D. J. James,[16] N. Jeffrey,[15] T. Jeltema,[48] R. Kessler,[31,32] O. Lahav,[15] J. Lee,[40] S. Lee,[51] C. Lidman,[52,9] H. Lin,[6] M. Lin,[40] J. L. Marshall,[53] J. Mena-Fernández,[41] R. Miquel,[54,26] J. Muir,[55,56] A. Möller,[57] R. C. Nichol,[11] A. Palmese,[58] M. Paterno,[6] W. J. Percival,[42,56] A. Pieres,[4,59] A. A. Plazas Malagón,[17,18] B. Popovic,[2] A. Porredon,[10,60] J. Prat,[31,61] H. Qu,[40] M. Raveri,[22] M. Rodriguez-Monroy,[45] A. K. Romer,[62] E. S. Rykoff,[17,18] M. Sako,[40] S. Samuroff,[13,26] E. Sanchez,[10] D. Sanchez Cid,[10,8] D. Scolnic,[2] I. Sevilla-Noarbe,[10] P. Shah,[15] E. Sheldon,[19] M. Smith,[63] E. Suchyta,[64] M. Sullivan,[65] M. E. C. Swanson,[3] B. O. Sánchez,[66,2] G. Tarle,[7] G. Taylor,[9] D. Thomas,[11] C. To,[31] L. Toribio San Cipriano,[10] M. Toy,[65] M. A. Troxel,[2] D. L. Tucker,[6] V. Vikram,[67] M. Vincenzi,[68] A. R. Walker,[1] N. Weaverdyck,[69,70] J. Weller,[71,72] P. Wiseman,[65] M. Yamamoto,[73,2] and B. Yanny[6]

(DES Collaboration)[*]

[1]*Cerro Tololo Inter-American Observatory, NSF's National Optical-Infrared Astronomy Research Laboratory, Casilla 603, La Serena, Chile*
[2]*Department of Physics, Duke University, Durham, North Carolina 27708, USA*
[3]*Center for Astrophysical Surveys, National Center for Supercomputing Applications, 1205 West Clark Street, Urbana, Illinois 61801, USA*
[4]*Laboratório Interinstitucional de e-Astronomia - LIneA, Avenida Pastor Martin Luther King Jr, 126 Del Castilho, Nova América Offices, Torre 3000/sala 817 CEP: 20765-000, Brazil*
[5]*Institute of Space Sciences (ICE, CSIC), Campus UAB, Carrer de Can Magrans, s/n, 08193 Barcelona, Spain*
[6]*Fermi National Accelerator Laboratory, P. O. Box 500, Batavia, Illinois 60510, USA*
[7]*Department of Physics, University of Michigan, Ann Arbor, Michigan 48109, USA*
[8]*Physik-Institut, University of Zürich, Winterthurerstrasse 190, CH-8057 Zürich, Switzerland*
[9]*The Research School of Astronomy and Astrophysics, Australian National University, Canberra, ACT 2601, Australia*
[10]*Centro de Investigaciones Energéticas, Medioambientales y Tecnológicas (CIEMAT), Madrid, Spain*
[11]*Institute of Cosmology and Gravitation, University of Portsmouth, Portsmouth, PO1 3FX, United Kingdom*
[12]*Physics Department, 2320 Chamberlin Hall, University of Wisconsin-Madison, 1150 University Avenue, Madison, Wisconsin 53706-1390, USA*
[13]*Department of Physics, Northeastern University, Boston, Massachusetts 02115, USA*
[14]*University Observatory, Faculty of Physics, Ludwig-Maximilians-Universität, Scheinerstraße 1, 81679 Munich, Germany*
[15]*Department of Physics & Astronomy, University College London, Gower Street, London, WC1E 6BT, United Kingdom*
[16]*Center for Astrophysics | Harvard & Smithsonian, 60 Garden Street, Cambridge, Massachusetts 02138, USA*
[17]*Kavli Institute for Particle Astrophysics & Cosmology, P. O. Box 2450, Stanford University, Stanford, California 94305, USA*
[18]*SLAC National Accelerator Laboratory, Menlo Park, California 94025, USA*
[19]*Brookhaven National Laboratory, Bldg 510, Upton, New York 11973, USA*
[20]*Instituto de Física Teórica, Universidade Estadual Paulista, São Paulo, Brazil*
[21]*School of Mathematics and Physics, University of Queensland, Brisbane, QLD 4072, Australia*
[22]*Department of Physics, University of Genova and INFN, Via Dodecaneso 33, 16146, Genova, Italy*
[23]*Instituto de Astrofisica de Canarias, E-38205 La Laguna, Tenerife, Spain*

2470-0010/2026/113(6)/063530(31)

[24]Universidad de La Laguna, Departamento Astrofísica, E-38206 La Laguna, Tenerife, Spain
[25]Korea Astronomy and Space Science Institute, 776 Daedeok-daero, Yuseong-gu, Daejeon 34055, South Korea
[26]Institut de Física d'Altes Energies (IFAE), The Barcelona Institute of Science and Technology, Campus UAB, 08193 Bellaterra (Barcelona), Spain
[27]Institut d'Estudis Espacials de Catalunya (IEEC), 08034 Barcelona, Spain
[28]Physics Department, William Jewell College, Liberty, Missouri 64068, USA
[29]School of Physics and Astronomy, Sun Yat-Sen University, 2 Daxue Road, Tangjia, Zhuhai 519082, China
[30]CSST Science Center for the Guangdong-Hongkong-Macau Greater Bay Area, SYSU, Zhuhai 519082, China
[31]Department of Astronomy and Astrophysics, University of Chicago, Chicago, Illinois 60637, USA
[32]Kavli Institute for Cosmological Physics, University of Chicago, Chicago, Illinois 60637, USA
[33]Jodrell Bank Center for Astrophysics, School of Physics and Astronomy, University of Manchester, Oxford Road, Manchester, M13 9PL, United Kingdom
[34]University of Nottingham, School of Physics and Astronomy, Nottingham NG7 2RD, United Kingdom
[35]Astronomy Unit, Department of Physics, University of Trieste, via Tiepolo 11, I-34131 Trieste, Italy
[36]INAF-Osservatorio Astronomico di Trieste, via G. B. Tiepolo 11, I-34143 Trieste, Italy
[37]Institute for Fundamental Physics of the Universe, Via Beirut 2, 34014 Trieste, Italy
[38]Hamburger Sternwarte, Universität Hamburg, Gojenbergsweg 112, 21029 Hamburg, Germany
[39]Department of Physics, IIT Hyderabad, Kandi, Telangana 502285, India
[40]Department of Physics and Astronomy, University of Pennsylvania, Philadelphia, Pennsylvania 19104, USA
[41]Université Grenoble Alpes, CNRS, LPSC-IN2P3, 38000 Grenoble, France
[42]Department of Physics and Astronomy, University of Waterloo, 200 University Ave W, Waterloo, Ontario N2L 3G1, Canada
[43]California Institute of Technology, 1200 East California Blvd, MC 249-17, Pasadena, California 91125, USA
[44]Institute of Theoretical Astrophysics, University of Oslo, P.O. Box 1029 Blindern, NO-0315 Oslo, Norway
[45]Instituto de Fisica Teorica UAM/CSIC, Universidad Autonoma de Madrid, 28049 Madrid, Spain
[46]Department of Astronomy, University of Illinois at Urbana-Champaign, 1002 W. Green Street, Urbana, Illinois 61801, USA
[47]Department of Astronomy, University of Geneva, ch. d'Écogia 16, CH-1290 Versoix, Switzerland
[48]Santa Cruz Institute for Particle Physics, Santa Cruz, California 95064, USA
[49]Center for Cosmology and Astro-Particle Physics, The Ohio State University, Columbus, Ohio 43210, USA
[50]Department of Physics, The Ohio State University, Columbus, Ohio 43210, USA
[51]Jet Propulsion Laboratory, California Institute of Technology, 4800 Oak Grove Dr., Pasadena, California 91109, USA
[52]Centre for Gravitational Astrophysics, College of Science, The Australian National University, Canberra, ACT 2601, Australia
[53]George P. and Cynthia Woods Mitchell Institute for Fundamental Physics and Astronomy, and Department of Physics and Astronomy, Texas A&M University, College Station, Texas 77843, USA
[54]Institució Catalana de Recerca i Estudis Avançats, E-08010 Barcelona, Spain
[55]Department of Physics, University of Cincinnati, Cincinnati, Ohio 45221, USA
[56]Perimeter Institute for Theoretical Physics, 31 Caroline Street North, Waterloo, Ontario N2L 2Y5, Canada
[57]Centre for Astrophysics & Supercomputing, Swinburne University of Technology, Victoria 3122, Australia
[58]Department of Physics, Carnegie Mellon University, Pittsburgh, Pennsylvania 15312, USA
[59]Observatório Nacional, Rua Gal. José Cristino 77, Rio de Janeiro, RJ - 20921-400, Brazil
[60]Ruhr University Bochum, Faculty of Physics and Astronomy, Astronomical Institute, German Centre for Cosmological Lensing, 44780 Bochum, Germany
[61]Nordita, KTH Royal Institute of Technology and Stockholm University, Hannes Alfvéns väg 12, SE-10691 Stockholm, Sweden
[62]Department of Physics and Astronomy, Pevensey Building, University of Sussex, Brighton, BN1 9QH, United Kingdom
[63]Physics Department, Lancaster University, Lancaster, LA1 4YB, United Kingdom

[64]*Computer Science and Mathematics Division, Oak Ridge National Laboratory, Oak Ridge, Tennessee 37831, USA*
[65]*School of Physics and Astronomy, University of Southampton, Southampton, SO17 1BJ, United Kingdom*
[66]*Aix Marseille Univ, CNRS/IN2P3, CPPM, Marseille, France*
[67]*Department of Physics, Central University of Kerala, Kasaragod, Kerala, India*
[68]*Department of Physics, University of Oxford, Denys Wilkinson Building, Keble Road, Oxford OX1 3RH, United Kingdom*
[69]*Berkeley Center for Cosmological Physics, UC Berkeley, California 94720, USA*
[70]*Lawrence Berkeley National Laboratory, 1 Cyclotron Road, Berkeley, California 94720, USA*
[71]*Max Planck Institute for Extraterrestrial Physics, Giessenbachstrasse, 85748 Garching, Germany*
[72]*Universitäts-Sternwarte, Fakultät für Physik, Ludwig-Maximilians Universität München, Scheinerstraße 1, 81679 München, Germany*
[73]*Department of Astrophysical Sciences, Princeton University, Peyton Hall, Princeton, New Jersey 08544, USA*

(Received 31 March 2025; revised 31 October 2025; accepted 30 January 2026; published 12 March 2026)

The Dark Energy Survey (DES) recently released the final results of its two principal probes of the expansion history: Type Ia supernovae (SNe) and baryonic acoustic oscillations (BAO). In this paper, we explore the cosmological implications of these data in combination with external cosmic microwave background (CMB), big bang nucleosynthesis (BBN), and age-of-the-Universe information. The BAO measurement, which is $\sim 2\sigma$ away from *Planck* 's ΛCDM predictions, pushes for low values of $\Omega_{\rm m}$ compared to *Planck*, in contrast to SN which prefers a higher value than *Planck*. We identify several tensions among datasets in the ΛCDM model that cannot be resolved by including either curvature ($k\Lambda$CDM) or a constant dark energy equation of state (wCDM). By combining BAO + SN + CMB despite these mild tensions, we obtain $\Omega_k = -5.5^{+4.6}_{-4.2} \times 10^{-3}$ in $k\Lambda$CDM, and $w = -0.948^{+0.028}_{-0.027}$ in wCDM. In wCDM, BAO and SN push again in different directions of parameter space, favoring, respectively, $w < -1$ and $w > -1$. If we open the parameter space to $w_0 w_a$CDM [where the equation of state of dark energy varies as $w(a) = w_0 + (1-a)w_a$], all the datasets are mutually more compatible, and we find concordance in the $[w_0 > -1, w_a < 0]$ quadrant, with BAO pushing for $w_a < 0$ and SN for $[w_0 > -1, w_a < 0]$. For DES BAO and SN in combination with *Planck* -CMB, we find a 3.2σ deviation from ΛCDM, with $w_0 = -0.673^{+0.098}_{-0.097}$, $w_a = -1.37^{+0.51}_{-0.50}$, a Hubble constant of $H_0 = 67.81^{+0.96}_{-0.86}\,{\rm km\,s^{-1}\,Mpc^{-1}}$, and an abundance of matter of $\Omega_{\rm m} = 0.3109^{+0.0086}_{-0.0099}$. For the combination of all the background cosmological probes considered (including CMB's angular acoustic scale $\theta_\star$), we still find a deviation of 2.8σ from ΛCDM in the $w_0 - w_a$ plane. Assuming a minimal neutrino mass, this work provides tentative evidence for non-ΛCDM physics, which is consistent with recent claims in support of evolving dark energy, or a source of unknown systematics.

DOI: 10.1103/z2q4-qcdq

I. INTRODUCTION

The Dark Energy Survey (DES) was designed as a multiprobe experiment to constrain properties of the dark energy and other cosmological parameters [1–4]. For that, it observed the DES wide field, nearly $5,000\ {\rm deg}^2$ of the southern sky, over six years (2013–2019) with five filters ($grizY$) to a depth of $i = 23.8$ [5]. In parallel, the DES supernova program (DES-SN) was repeatedly observed with a 5/6 night cadence of ten $\sim 3\ {\rm deg}^2$ fields for five ~ 6 month seasons.

Two analyses of the main cosmology probes from the final DES dataset were recently published: the baryonic acoustic oscillations (BAO) and type Ia supernova (SNe Ia) analyses. DES measured the angular BAO feature from the clustering of ~ 16 million galaxies to determine the ratio of the angular distance to the sound horizon with a precision of 2.1% at $z_{\rm eff} = 0.85$ [6,7]. Additionally, DES measured the luminosity distance to redshift relation from 1,635 high-redshift photometrically classified SNe Ia, hereafter referred to as DES-SN5YR [8]. That paper along with [9] explored in detail the implications of DES SNe for the cosmological model. In the near future, DES will release results from other principal cosmological probes using the final dataset, such as the combination of galaxy clustering and weak lensing, galaxy cluster number counts, and cross-correlation with external datasets. For many of those probes, DES work based on previous data releases are considered the state-of-the-art [10–17]. Both SN and BAO represent measurements of the homogeneous properties of

[*]Contact author: des-publication-queries@fnal.gov

the Universe and are only sensitive to the expansion history (as opposed to properties that probe the distribution and evolution of inhomogeneities). We refer to these probes as measurements of the cosmological background. On the other hand, the remaining DES probes will be sensitive to spatial perturbations and thus, to the history of growth of structure in the Universe.

In the last year (2024), a lot of attention has been paid to tensions of current data with the standard cosmological model, (flat) ΛCDM, at the background level, in particular when allowing the equation of state of dark energy (w) to evolve. Typically, this is reported via the CPL parametrization (named for the authors of [18,19]), where the equation of state is assumed to evolve linearly with the scale factor a: $w(a) = w_0 + w_a(1 - a)$. First, DES-SN5YR reported a $\sim 2\sigma$ deviation in the $w_0 - w_a$ parameter plane [8]. Furthermore, the DES-Y6-BAO measurement of D_M/r_d at $z_{\rm eff} = 0.85$ showed a 2.1σ deviation from the value predicted by *Planck* in the (flat) ΛCDM model, though that paper did not evaluate the impact on cosmological parameters. Finally, the DESI 2024 BAO results showed a tension with ΛCDM [20]: when DESI BAO [21,22] is combined with DES SN and Planck CMB, the reported tension in the $w_0 - w_a$ plane increases to 3.9σ with ΛCDM. The significance of the deviation from ΛCDM remains at a similar level when considering DESI's full-shape analysis [23], which includes information from the growth of structure.

In this context, this paper has several goals. First, we aim to understand how the 2.1σ deviation of the DES-Y6-BAO translates to cosmological parameters in ΛCDM and simple extensions (kΛCDM, wCDM, νΛCDM). Second, we demonstrate the power of combining the two DES background probes, BAO and SN, as well as what insight they together can contribute to the current investigations of evolving dark energy.[1] For this, we combine and compare our data with other background probes such as big bang nucleosynthesis (BBN), direct H_0 measurements from SH0ES, the age of the Universe, and the angular scale of the sound horizon, $\theta_\star$, as seen by *Planck*. We will also combine our data with primary CMB probes (temperature and polarization: TT + TE + EE). The CMB is the only probe considered here that contains information beyond the background expansion level. External probes that are more sensitive to nonlinear structure growth, such as CMB-lensing and redshift space distortions, are not considered in this work and will be compared in the future to other DES growth of structure probes (cosmic shear, galaxy clustering, cluster counts, etc.).

The paper is organized as follows. We describe the different probes considered in Sec. II. The methodology for cosmology inferences in described in Sec. III. We then present the results in Sec. IV. Discussion and conclusion are presented in Secs. V and VI, respectively.

II. DATA

A. DES Y6 BAO

The Dark Energy Survey released the baryonic acoustic oscillations analysis from the final dataset (Y6, which spans six years of data) in [6], which builds upon the Y1 [25] and Y3 analyses [26]. For that work, we built a BAO-optimized sample in the redshift range $0.6 \lesssim z \lesssim 1.2$, where DES could obtain the most competitive constraints [7]. The BAO sample was defined using a red and bright selection and is made up of $\sim$16 million galaxies from a $\sim 4,300\ {\rm deg}^2$ area. This sample was split into six tomographic bins based on photometric redshift $z_{\rm ph}$[2] with width $\Delta z_{\rm ph} = 0.1$. The redshift distribution of each bin is estimated using a combination of directional neighboring fitting (DNF [27]), clustering redshifts [28], and direct calibration with spectra from VIPERS [29]. Spurious density correlations with foregrounds and observing conditions are corrected with linear weights via the iterative systematic decontamination (ISD) method [12,30]. More details about the BAO sample and its calibration can be found in [7], which uses a methodology based on that from Y1 [31] and Y3 [32].

1. Fiducial BAO: Angular BAO in $0.6 < z_{\rm ph} < 1.2$ *(BAO)*

The DES Y6 BAO analysis measured the angular BAO feature from three different estimators of galaxy clustering: the angular correlation function [ACF or $w(\theta)$, [33]), the angular power spectrum (APS or C_ℓ, [34]) and the projected correlation function [PCF or $\xi_p(s_\perp)$, [35–37]]. In all three cases, we analyzed the six tomographic bins simultaneously by fitting a single angular BAO shift parameter,

$$\alpha = (D_M/r_d)/(D_M/r_d)_{\rm fid}. \qquad (1)$$

The methods were validated against $\sim 2,000$ ICE-COLA mock catalogs (built using the methodology from [38–41]) and checked for robustness against variations in assumptions about the galaxy redshift distributions. From this validation, we obtained a small contribution of systematic error that was added in quadrature to the final statistical error bars.

The angular BAO shift parameter α was measured in a blind analysis: its inferred value was concealed and only revealed after performing a series of tests. These tests

[1] A recent paper, [24], also explored this combination. The two main differences with that analysis are that we do not include CMB-lensing (see Sec. II C), and we consider a baseline metric for deviations from ΛCDM that is sensible for non-Gaussian likelihoods, as opposed to that based on $\Delta\chi^2$, as discussed in Sec. III C 1. In addition, we explore many probe combinations (beyond the baseline BAO + SN + CMB) and several expansion history models.

[2] $z_{\rm ph}$ is the main redshift estimate of the DNF photometric redshift algorithm.

included showing that the α inference was robust to partial data removal (e.g., redshift splits), method variations (e.g., scale choices), different data calibration choices (e.g., redshifts, systematic weights) and between the three summary statistics (ACF, APS, PCF, and their combination).

Finally, the likelihood of the angular BAO shift from the three estimators (ACF, APS, and PCF) is combined into a single likelihood for α, which is close to a Gaussian approximation yielding

$$D_M(z_{\rm eff} = 0.85)/r_d = 19.51 \pm 0.41. \quad (2)$$

For the purposes of this paper, we employ the full likelihood reported in [6], in the form of an interpolated table of χ^2 versus α. All results using this likelihood are labeled as "BAO". All the data products associated to this paper are publicly available.[3]

This is our fiducial BAO constraint and is represented in red in Fig. 1 at the effective redshift of our sample, $z_{\rm eff} = 0.85$. This value is found to be 2.1σ and 4.3% below the prediction of $D_M(z_{\rm eff} = 0.85)/r_d = 20.39$ given by the *Planck* ΛCDM best fit, and represented by the black line in Fig. 1.

2. Alternative BAO: Individual $\Delta z_{\rm ph} = 0.1$ tomographic bins (BAO-5)

As a supplement to our main BAO analyses, we also consider an alternative BAO likelihood with shift parameters α estimated separately for each of the individual $\Delta z_{\rm ph} = 0.1$ tomographic bins. This builds on [6], in which these binned α values were determined. Although each of the individual bins will have a lower signal-to-noise ratio than their combination, having several measurements of the distance-redshift relation could potentially resolve features in the expansion history not revealed by a single point. This motivates us to investigate the possibility in this paper, though these are not considered fiducial results because they were not subject to the same level of validation as the single-bin BAO studies.

More specifically, the alternative version of the BAO likelihood is based on the ACF in the thin $\Delta z_{\rm ph} = 0.1$ bins. The methodology to obtain this likelihood is explained in detail in Appendix B. There, we compute the systematic errors (from modeling and redshifts) associated with each redshift bin and the covariance of their α measurements, since they overlap slightly in redshift. We do not consider the APS and PCF methods in this case, since they are found to be less robust for individual redshift bins. The resulting likelihood consists of five angular BAO points represented in orange in Fig. 1 with a correlation matrix shown in Fig. 12. There are five rather than six measurements

[3] https://des.ncsa.illinois.edu/releases/y6a2/Y6bao.

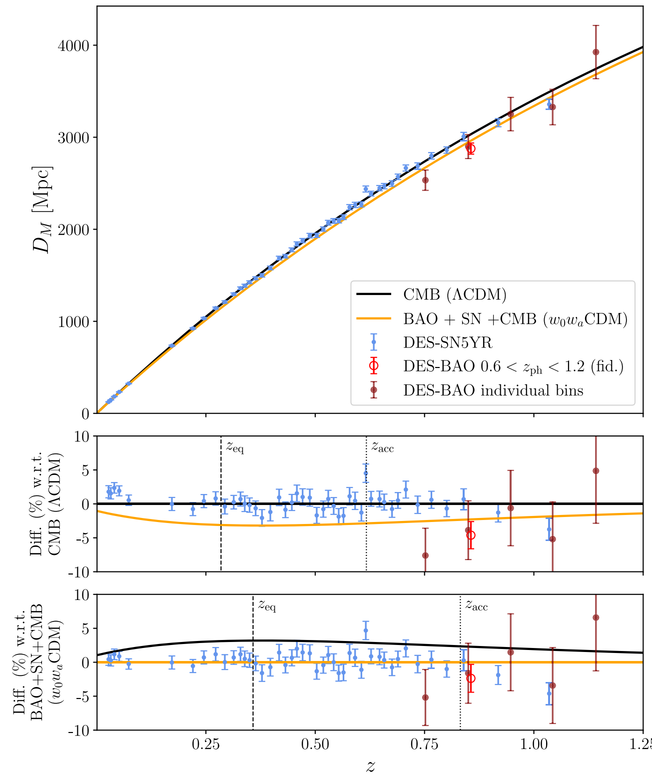

FIG. 1. Illustration of the distance-redshift relation from DES compared to the best-fit CMB-ΛCDM and BAO + SN + CMB-w_0w_aCDM predictions. We show the (comoving) angular distance $D_M(z)$ from DES BAO results both from our fiducial single-bin measurement (evaluated at an effective redshift of $z_{\rm eff} = 0.85$ by fitting all the data in $0.6 < z_{\rm ph} < 1.2$) but also the alternative 5-bin split measurements (with individual bins of $\Delta z_{\rm ph} = 0.1$). In this figure, for BAO, we assume a value of $r_d = 147.46$ Mpc (see Sec. II C 3). We also show the SN binned results, for which we plot the luminosity distance transformed to angular distance using Eq. (14) for the 1829 SNe in DES-SN5YR (1635 DES SNe + 194 low-z SNe from external samples). To obtain the SN distances we calibrate the SN absolute magnitude $\mathcal{M}$ such that the residuals with respect to the given cosmology average to zero. This calibration is different by $\delta\mathcal{M} \sim 0.06$ for the two cosmologies, and hence, we show in the lower panels two residual plots, one with SNe calibrated to CMB-only ΛCDM (this calibration is also used in the upper panel) and the other calibrated to the best-fit w_0w_aCDM model for the BAO + SN + CMB data combination. The residual plot shows the percentage difference in $D_M(z)$ compared to the best fit. The 1829 SNe are binned with equal numbers in each bin (with the D_M and z shown being the average weighted by the inverse variance of D_M). The w_0w_aCDM model fits better the $z < 0.1$ SNe and the $z \gtrsim 0.75$ BAO and SN data. We also include two vertical lines to indicate the redshift of matter-dark energy equality ($z_{\rm eq}$, dashed) and the redshift when acceleration starts ($z_{\rm acc}$, dotted) for each the two models. This figure illustrates in a simplified way how BAO and SN together constrain the expansion history models; however, in our analyses, both $\mathcal{M}$ and r_d are varied.

because the lowest redshift bin ($0.6 < z_{\rm ph} < 0.7$) does not show a detection of BAO. As studied in [6], given the lower SNR of the individual bins, finding one nondetection is not unexpected. From our ∼2000 simulations, we found that >25% of them show at least one bin with a nondetection.

We find that the redshift-binned α measurements fluctuate with redshift, with some apparent trend with redshift. Although these were found to be compatible with statistical fluctuations, in order to test whether they could be hinting at a feature in the expansion history of the Universe, we ran a few analyses substituting our fiducial BAO likelihood ($0.6 < z_{\rm ph} < 1.2$) with the alternative individual-bin BAO, labeled as BAO-5. As we found a negligible impact on the cosmological parameters, we will not discuss these individual-bin BAO measurements in the main text, but we do report the results in Appendix C.

B. DES-SN5YR (SN)

The Dark Energy Survey released the Hubble diagram from the sample of SNe Ia discovered and measured during the full five years of the DES-SN program in [8]. The DES-SN survey detected over 30,000 SN candidates over 5 years of observations and made a classification based only on photometry. From these, 1,635 were deemed high-quality SNe Ia-like, had spectroscopically measured redshifts from their host galaxies, and are included in the Hubble diagram with a weight inversely proportional to their probability of being a type Ia SN, as given by the machine-learning classifier SuperNNova [42–44]. The Hubble diagram also includes 194 spectroscopically confirmed low-z ($z < 0.1$) SNe Ia from external surveys. For the cosmological analyses in this paper, these two subsamples are used together, simply labeled as SN, and are shown in redshift bins as blue points in Fig. 1.

A series of papers describe the details of the DES-SN5YR analysis, itself built upon the interim DES-SN3YR analysis of spectroscopically confirmed SNe [45]. The processing and calibration of DES SN light curves are described by [46,47]. SN light-curve fitting and standardization as well as the estimation of the final SN distance moduli are presented by [44,48]. Host galaxy properties are presented in [49] based on deep coadd imaging of the SN fields [50]. Finally, [44] provides a detailed description of all the sources of systematics included in the final DES-SN5YR uncertainty covariance matrix.

In the DES-SN5YR analysis, SN standardized distances $\mu_{\rm obs}$ are estimated as

$$\mu_{\rm obs} = m_x + \alpha\, x_1 - \beta\, c + \gamma\, G_{\rm host}(M_\star) - M - \Delta\mu_{\rm bias}, \quad (3)$$

where m_x, x_1, and c are the fitted amplitude, stretch and color of each SN. α, β and γ are global nuisance parameters. $\Delta\mu_{\rm bias}$ are distance corrections applied to take into account the effects of sample selection, calibrated as a function of the properties of the SN and host galaxy. $G_{\rm host}$ is an environmental adjustment taking the form of a step function depending on the stellar mass of the SN host, $M_\star$. These parameters are calibrated and validated in the characterization of the SN sample in the studies cited above. Finally, the SN fiducial absolute magnitude M is degenerate with the Hubble constant H_0 and is combined into a single parameter $\mathcal{M} = M + 5\log_{10}(c/H_0)$, which is (analytically) marginalized over in the SN likelihood [8].

The SN distances $\mu_{\rm obs}$ and associated statistical and systematic covariance matrices are publicly available.[4]

C. *Planck* CMB

1. Temperature and polarization anisotropy (CMB)

We incorporate measurements of the CMB temperature and polarization anisotropies using the *Planck* 2018 likelihood [51], which we will subsequently refer to using the label “CMB”. Specifically, for temperature and polarization spectra for $\ell \geq 30$, we employ the `Plik-lite` likelihood, which incorporates the effects of marginalizing over *Planck* foreground and nuisance parameters and includes measurements of spectra up to $\ell_{\rm max} = 2508$ for TT, and $\ell_{\rm max} = 1996$ for TE and EE. Following the standard *Planck* analysis, at low multipoles ($2 \leq \ell < 30$), we use the `Commander` likelihood for the TT spectrum and the `SimAll` likelihood for the EE polarization spectrum. We do not include CMB lensing constraints.

When including this CMB likelihood, we fit several additional parameters compared to our background-only studies. These include $A_{\rm s}$ and $n_{\rm s}$, the amplitude and slope of the primordial power curvature spectrum, as well as the optical depth τ. We additionally marginalize over the total *Planck* calibration a_{Planck} as a nuisance parameter. The priors used for these parameters can be found in Table I.[5]

2. Angular scale of the acoustic peak ($\theta_\star$)

In order to isolate geometric/background information from the CMB, in some cases, we instead consider a constraint on

$$\theta_\star = r_s(z_\star)/D_M(z_\star), \quad (4)$$

[4]https://github.com/des-science/DES-SN5YR.

[5]Note that this implementation of the CMB likelihood is slightly different than what was used in the DES-SN5YR analysis of [8], which uses a python implementation of the *Planck* likelihood described in [52]. At $\ell \geq 30$, that implementation is identical to what is used in this paper, but it differs at low-ℓ. The DES-SN5YR analysis uses a Gaussian approximation for low-ℓCMB temperature and includes a Gaussian prior on τ instead of low-ℓ polarization data. While we expect these choices to have a negligible impact on our conclusions, they may induce slight differences between SN + CMB constraints reported in this paper and in [8].

TABLE I. Sampled parameters and priors used in the ΛCDM, kΛCDM, wCDM, w_0w_aCDM, and νΛCDM analyses. When including CMB data, we additionally vary the parameters listed in the bottom section. Square brackets denote a flat prior, while parentheses denote a Gaussian prior of the form $\mathcal{N}(\mu, \sigma)$, with μ and σ being the mean and standard deviation, respectively. The parameter $\sum m_\nu$ is fixed to 0.06 eV for all models other than νΛCDM.

Parameter	Prior
ΛCDM	
H_0 [km s^{-1} Mpc^{-1}]	[55, 91]
$\Omega_{\rm m}$	[0.1, 0.9]
$\Omega_{\rm b}$	[0.03, 0.07]
***k*ΛCDM**	
Ω_k	[−0.25, 0.25]
***w*CDM**	
w	[−3, −0.33]
w_0w_aCDM	
w_0	[−3, −0.33]
w_a	[−3, 3]
νΛCDM	
$\sum m_\nu [eV]$	[0, 1]
Chains that include CMB	
τ	[0.04, 0.15]
$A_{\rm s} \times 10^9$	[0.5, 5.0]
$n_{\rm s}$	[0.87, 1.07]
$a_{\rm Planck}$	(1.0, 0.0025)

the ratio between the baryon-photon sound horizon and the comoving distance at the redshift of recombination, $z_\star$. We incorporate this via a Gaussian likelihood taken from the same *Planck* 2018 temperature and polarization data described above, [53], having

$$100\,\theta_\star = 1.04109 \pm 0.00030. \tag{5}$$

For ease of comparison, we note that the $\theta_\star$ likelihood used in DESI analyses [20] has a nearly identical mean based on *Planck* 2018 constraints which include lensing, but DESI additionally increased this width by 75% to account for possible modeling uncertainties.

3. Comoving scale of the acoustic peak (r_d)

Along with constraints on the parameters of specific cosmological models, we will consider a cosmographic expansion to measure H_0 (Sec. IV F). For this study, we incorporate a measurement of the comoving scale of the acoustic peak, r_d. This quantity is the maximum distance that sound waves could travel in the early Universe before photons and baryons decoupled from each other. It depends on the baryon density and total matter density in the early Universe.

When this constraint is applied, we use a Gaussian prior on the sound horizon given by

$$r_d = 147.46 \pm 0.28 \text{ Mpc}. \tag{6}$$

This value was determined using chains from [54], which are based on *Planck* PR4 data and incorporate information from the CMB in a way that removes late-time cosmology dependence associated with the late-integrated Sachs-Wolfe effect, the optical depth to reionization, CMB lensing and foregrounds.

D. Age of the Universe ($t_{\rm U}$)

To further inform our w_0w_aCDM analysis, particularly for understanding how its additional degrees of freedom affect the expansion history, we additionally consider a prior on the age of the Universe, $t_{\rm U}$, inferred from observations of globular clusters. The age of the Universe, $t_{\rm U}$, has been historically used to provide a prior on cosmological parameters, primarily through its inverse proportionality to H_0, although there is dependence on other cosmological parameters [see Eq. (15)]. It is interesting to revisit this in light of new data and extended cosmological models. We use a result derived from the color-magnitude diagrams of globular clusters in the Milky Way.

Globular clusters are metal-poor stellar systems that formed early in the Universe. Historically, their ages (by definition younger than the age of the Universe) were determined by examining the main sequence turnoff and comparing it to results from stellar modeling codes [55]. Systematics arise from uncertainty in stellar modeling codes (especially in relation to convection), extinction, metallicity, blending effects, uncertain distances to the clusters, nuclear reaction rates, and whether they arise from single or multiple populations.

Modern methodologies attempt to control for these systematics by fitting the entire color-magnitude diagram in a Bayesian framework, with marginalization over parameters describing some of the systematics [56]. In this way, a simultaneous determination is made of age, metallicity, distance, and absorption to each cluster, which may be checked for consistency with other data (for example, parallax-derived distances to the cluster). Whether the cluster contains a single or multiple populations (which in principle could have different ages) may be checked by examining the posterior distribution of the metallicity of the cluster as populations originating at different times may have different metallicities.

We use the results of [56], who combined the posteriors of the ages of the 38 most metal-poor clusters (presumed to be the oldest). This was convolved with a reasonable prior probability density of its formation time, derived from assuming the clusters formed at redshift $z > 11$ [57]. Although there is some cosmological dependence implicit in the conversion from formation redshift to formation time, it is small compared to other sources of error, and therefore it may be used to constrain nonstandard cosmologies in addition to ΛCDM. We therefore use the Gaussian prior given by

$$t_{\mathrm{U}} = 13.5 \pm 0.52\ \mathrm{Gyr}, \quad (7)$$

where the error combines statistical and systematic sources, with the highest error contribution arising from uncertain nuclear reaction rates. This is compatible with the *Planck* estimate of $t_{\mathrm{U}} = 13.797 \pm 0.023$ Gyr within ΛCDM (Table 2 of [53]). When implementing it, we impose this as a Gaussian prior as a post-processing of the equivalent chains without this prior. We describe the methodology further in Sec. III B.

E. Big bang nucleosynthesis (BBN)

Big bang nucleosynthesis (BBN) theory predicts the abundance of light elements in the early Universe, such as deuterium and helium, as well as their relation to the baryon-to-photon ratio. Therefore, the observational determination of the primordial deuterium abundance and the helium fraction can be used to compute the physical baryon density parameter at present, $\Omega_{\mathrm{b}}h^2$, where $h \equiv H_0/(100\ \mathrm{km\,s^{-1}\,Mpc^{-1}})$ (see [58,59] for further details).

The resulting constraints on $\Omega_{\mathrm{b}}h^2$ depend on the modeling of underlying nuclear interactions. We employ a BBN constraint from a recent analysis [60] that recalculates the predictions while marginalizing over uncertainties in reaction rates. It reports a conservative constraint of

$$\Omega_{\mathrm{b}}h^2 = 0.02218 \pm 0.00055. \quad (8)$$

This is the same BBN Gaussian prior on $\Omega_{\mathrm{b}}h^2$ used for the cosmological inference from the BAO measurement in the DESI 2024 analysis [20].

F. Direct measurement of the Hubble constant (direct H_0)

The SH0ES Collaboration has recently used observations from the Hubble Space Telescope (HST) of Cepheid variable stars in the host galaxies of 42 type Ia SNe to calibrate the Hubble constant. This analysis is described in [61], where they find

$$H_0 = 73.04 \pm 1.04\ \mathrm{km\,s^{-1}\,Mpc^{-1}}, \quad (9)$$

as their baseline result. Here, we do not include this value in any of our analyses, but we rather consider its comparison to our derived H_0 values on several occasions throughout the paper.

There is an ongoing debate about the value of H_0. In particular, direct calibration methods such as the one quoted above tend to prefer a higher value than those using CMB or other calibrations from the early Universe (). The measurement shown above is typically regarded as the consensus direct-H_0 measurement. A recent review on this topic can be found in [62].

III. METHODS

A. Background evolution

The main focus of this paper is to characterize the constraints of DES probes of the expansion history of the Universe: BAO and SN. We will often refer to these as *background* probes because they measure the background expansion upon which all other cosmological processes rest. Here, we briefly review the basic concepts around these observables and the expansion history of the Universe.

We consider four different models for the late-time expansion of the Universe. The first is the standard model, ΛCDM, which assumes flatness and a constant dark energy density given by $\Omega_\Lambda = (1 - \Omega_{\mathrm{m}})$. Second, we consider the kΛCDM model, with free curvature given by Ω_k. Third, the wCDM model includes a constant dark energy equation of state w as a free parameter, assuming flat geometry. Finally, we study the w_0w_aCDM model, where the dark energy equation of state evolves linearly with the scale factor,

$$w(a) = w_0 + w_a(1 - a). \quad (10)$$

Each of these models has a different parametrization of the late-time expansion history of the Universe as given by the Friedmann equation,[6]

$$\frac{H(a)^2}{H_0^2} = \begin{cases} \Omega_{\mathrm{m}}a^{-3} + (1 - \Omega_{\mathrm{m}}) & \text{for } \Lambda\mathrm{CDM} \\ \Omega_{\mathrm{m}}a^{-3} + (1 - \Omega_{\mathrm{m}})a^{-3(1+w)} & \text{for } w\mathrm{CDM} \\ \Omega_{\mathrm{m}}a^{-3} + (1 - \Omega_{\mathrm{m}})a^{-3(1+w_0+w_a)}e^{-3w_a(1-a)} & \text{for } w_0w_a\mathrm{CDM} \\ \Omega_{\mathrm{m}}a^{-3} + (1 - \Omega_{\mathrm{m}} - \Omega_k) + \Omega_k a^{-2} & \text{for } k\Lambda\mathrm{CDM} \end{cases}, \quad (11)$$

[6]We are neglecting in this equation the radiation term $\Omega_r a^{-4}$, which is only relevant for the early Universe. However, we do include radiation in calculations for the CMB constraints.

with H_0 the Hubble constant. The parenthesis in the second term represents the density parameter of dark energy (Ω_Λ in ΛCDM and kΛCDM), but this is not a free parameter, since we always need to ensure $\sum \Omega_i = 1$.

We additionally consider constraints on a flat ΛCDM cosmology with a nonminimal sum of neutrino masses, νΛCDM. As was recently highlighted in [63], while cosmological neutrinos are more commonly discussed in terms of how they impact structure formation, background probes like those we consider here are also sensitive to their mass. This is because the mass of neutrinos determines when they become nonrelativistic and thus, when they contribute to Eq. (11) as matter as opposed to radiation. Relatedly, the fact that neutrinos are relativistic at the time of recombination means that CMB constraints on matter density are primarily sensitive to CDM and baryons, while BAO and SN probe the total matter density—including neutrinos. Thus, together the CMB and probes of late-time expansion provide complementary information about neutrino mass. For the other cosmological models described above, we model a single massive neutrino species with its mass set to 0.06 eV, the minimum allowed by neutrino oscillation experiments. For νΛCDM, we model neutrinos with three degenerate mass species, varying the sum of their masses $\sum m_\nu$ as a free parameter.

The two key probes considered here rely on the distance-redshift relation, which depends on an integral over Eq. (11). The BAO feature serves as a standard ruler that constrains the comoving angular distance, which is given by

$$D_M = \frac{c}{H_0\sqrt{|\Omega_k|}} S_k\left[\int \sqrt{|\Omega_k|}\frac{dz}{H(z)/H_0}\right], \qquad (12)$$

with $S_{k=0}[x] \equiv x$, $S_{k<0}[x] \equiv \sin[x]$, and $S_{k>0}[x] \equiv \sinh[x]$, where k is the sign of Ω_k.

BAO observations constrain the ratio between D_M and the sound horizon r_d as follows. Baryonic acoustic oscillations are generated by sound waves in the early Universe that propagate in the photobaryon plasma until they decouple at the drag epoch, z_d. This leaves a preferred scale in the distribution of matter in the Universe, given by the sound horizon at that epoch,

$$r_d = \int_{z_d}^{\infty} \frac{c_s(z;\Omega_b h^2)}{H(z)} dz, \qquad (13)$$

where c_s is the sound speed. The fact that the sound speed depends on the physical density of baryons, $\Omega_b h^2$ means it will be interesting to combine BAO information with BBN constraints (Sec. II E). Complementary information can also be provided by the acoustic peak as detected in the CMB, which is sensitive to the sound horizon at a slightly different epoch (see Sec. II C 2).

SNe Ia are standardizable candles, which constrain the luminosity distance, related to angular distance by

$$D_L(z) = (1+z)D_M(z). \qquad (14)$$

This is typically transformed to the distance modulus $\mu(z) = 5\log_{10}(D_L(z)/10\ \mathrm{pc})$, which appears in Eq. (3). One thing to bear in mind is that we do not know *a priori* the actual absolute magnitude of SNe Ia, hence this quantity [$\mathcal{M}$ in Eq. (3)] is fully degenerate with H_0 in Eq. (11).

When using the priors on the age of the Universe (Sec. II D), from the definition of $H(t) = \dot{a}/a$, we compute

$$t_\mathrm{U} = \int_0^1 \frac{da}{aH(a)}. \qquad (15)$$

Considering this expression, we note that the w_0w_aCDM model is a parametrization that allows one to test whether time-varying dark energy is a better fit than a cosmological constant but is unlikely to be a true model down to $a \to 0$. However, since the impact on the age is largest at later times when the matter density is low, this calculation remains a useful framework in which to constrain the evolution of the expansion history $H(t)$ that would be too extreme in terms of observed stellar ages.

B. Parameter inference

To infer constraints on the parameters $\mathbf{p}$ given the data $\mathbf{D}$, we construct a posterior probability distribution following the Bayes' Theorem:

$$P(\mathbf{p}|\mathbf{D},M) \propto \mathcal{L}(\mathbf{D}|\mathbf{p},M)P(\mathbf{p}|M), \qquad (16)$$

where M is the assumed theoretical model, $P(\mathbf{p}|M)$ is a prior probability distribution on the parameters, and $\mathcal{L}$ is the likelihood function of the parameters given the data. The proportionality constant in Eq. (16) is given by the inverse of the Bayesian evidence,

$$P(\mathbf{D}|M) = \int \mathrm{d}\mathbf{p}\mathcal{L}(\mathbf{D}|\mathbf{p},M)P(\mathbf{p}|M). \qquad (17)$$

Under the Gaussian likelihood approximation, we can define $\mathcal{L}$ as

$$\mathcal{L}(\mathbf{D}|\mathbf{p},M) \propto e^{-\frac{1}{2}\chi^2}, \qquad (18)$$

where χ^2 is the goodness of fit of the model M to the data $\mathbf{D}$, given the data covariance. Throughout this work, we use the χ^2 or likelihood functions publicly released from each data set described in Sec. II. We do not assume any correlation between likelihood functions from different datasets.

The list of parameters sampled and the priors assumed for them is included in Table I. In addition to the priors listed, we impose the condition $w_0 + w_a < 0$ when considering the w_0w_aCDM model. This prior ensures $w(a) < 0$ at all redshifts, avoiding the parameter space for which there is no radiation domination era.

To implement a prior for the age of the Universe $t_{\rm U}$ (see Sec. II D), we exploit the fact that the prior P and the likelihood appear in combination in Eqs. (16) and (17). We may therefore implement the age prior by either multiplying P or the likelihood $\mathcal{L}$ by $P(t_{\rm U}) \sim \mathcal{N}(13.5, 0.52)$ Gyr [it is also required to renormalize P such that $\int \mathrm{d}\mathbf{p}P(\mathbf{p}|M) = 1$]. It is computationally convenient to adopt the former for posterior estimation (by reweighting chains) and the latter for evidence calculation (by adjusting the likelihood).

We sample the posterior distributions of the parameters using two different Monte Carlo nested samplers, POLYCHORD [64] and NAUTILUS [65], finding equivalent constraints with the two methods and using the former by default. We use the implementation of these two samplers available in the COSMOSIS[7] framework [66], which we use as our main inference pipeline throughout this work.[8] We use the CAMB Boltzmann solver [68,69] to compute the underlying background quantities and its HALOFIT Takahashi implementation for the nonlinear matter power spectrum [70,71] when including the CMB likelihood. For $k\Lambda$CDM chains including the CMB likelihood, since CAMB calculations can become significantly slower for $\Omega_k \neq 0$, we initially run the NAUTILUS sampler using lower-resolution CAMB settings, then importance sample the result with our fiducial pipeline to obtain a final posterior estimate.

When providing constraints, we report the mean in each parameter and use the GETDIST[9] package [72] to obtain equal-posterior credible regions (c. r.) and to plot the posterior distributions. The procedure for reporting credible regions is the following.

We examine the 68% credible regions and use their distance from the mean to determine (potentially asymmetric) 1σ errors. We then determine whether those bounds are close to the prior boundary, with closeness defined by assessing whether the distance between the boundary and the 68% credible region is smaller than that 1σ error bar. There are three different scenarios:

(1) *Both bounds are far from the prior boundaries:* If the 2σ region does not overlap with the prior boundary, we report two-sided errors.

(2) *One bound is close to a prior boundary:* If one of the 2σ bounds is close to the prior boundary, we report a one-sided 95% bound.

(3) *Both bounds are close to the prior boundaries:* If both 2σ bounds are close to the prior boundaries, we report no constraint.

[7] https://cosmosis.readthedocs.io/.

[8] With the exception of Sec. IV F, which uses the methodology described in [67].

[9] https://github.com/cmbant/getdist.

C. Tension metrics

Given the recent debate about possible evidence favoring dynamical dark energy over a cosmological constant, in this work, we will be especially interested in computing (1) deviations from the reference model, ΛCDM, and (2) tension between datasets. The methods to quantify these are laid out below.

1. *Quantifying deviations from* ΛCDM

To quantify preferences for an extended model relative to ΛCDM, we compare constraints on cosmological parameters. To do so, we compute the probability of a shift in the alternative model's added cosmological parameters relative to their corresponding ΛCDM values. This probability is defined as

$$\Delta(D, M) \equiv \int_{P(\mathbf{p}|D,M) > P(\mathbf{p}^*|D,M)} P(\mathbf{p}|D, M)\mathrm{d}\mathbf{p}, \qquad (19)$$

where $\mathbf{p}$ represents the additional parameters of the model M with respect to ΛCDM (e.g., w_0 and w_a in w_0w_aCDM), and $\mathbf{p}^*$ denotes the ΛCDM values of these parameters (e.g., $w_0 = -1$, $w_a = 0$). This integral quantifies the posterior mass exceeding the isodensity contour defined by the ΛCDM posterior value, $P(\mathbf{p}^*|D, M)$. Note that if the extra parameters have flat priors, as it is in the cases considered here, this result is parameter invariant.

To compute the integral in Eq. (19), we use the kernel density estimate (KDE) method described in [73]. In the remaining part of this section, we use the shorthand notation $P(\mathbf{p}) \equiv P(\mathbf{p}|D, M)$. Since we have posterior samples from P, the integral in Eq. (19) can be estimated as a Monte Carlo (MC) volume integral,

$$\hat{\Delta} = \frac{1}{\sum_{i=1}^{n} w_i} \sum_{i=1}^{n} w_i S(\hat{P}(\mathbf{p}_i) - \hat{P}(\mathbf{p}_i^*)), \qquad (20)$$

where $S(x)$ is the Heaviside step function, equal to unity for $x > 0$ and zero otherwise, n is the number of weighted samples $\mathbf{p}_i$ from P, and $\hat{P}$ represents their KDE estimates. Given that we are analyzing one- or two-dimensional posterior distributions, KDE evaluations can be efficiently performed using fast Fourier transforms (FFT) on a discrete grid, making the computation effectively instantaneous.

We always report results as the effective number of standard deviations. Given an event of probability Δ, it is given by [74],

$$n_\sigma \equiv \sqrt{2}\,\mathrm{Erf}^{-1}(\Delta). \qquad (21)$$

TABLE II. Statistical significance, in σs, of deviations from ΛCDM based on shifts in the additional parameter(s) in the extended model: Ω_k in $k\Lambda$CDM, w in wCDM and $\{w_0, w_a\}$ in w_0w_aCDM. See the methodology described in Sec. III C 1. For the case of $t_{\rm U}$ priors, we consider the fiducial Gaussian prior case and, in parenthesis, the case where only a lower bound on $t_{\rm U}$ is set. We highlight in bold the case for BAO + SN + CMB, our most constraining combination, which in the w_0w_aCDM model shows a 3.2σ deviation from ΛCDM.

	Deviations from ΛCDM (σ)		
Dataset	$k\Lambda$CDM	wCDM	w_0w_aCDM
BAO + SN + BBN	1.4	1.4	1.8
BAO + SN + BBN + $t_{\rm U}$	⋯	⋯	2.0 (2.7)
BAO + SN + $\theta_\star$	2.5	2.7	2.3
BAO + SN + $\theta_\star$ + BBN	2.8	3.1	2.8
BAO+SN+$\theta_\star$+BBN+$t_{\rm U}$	⋯	⋯	2.9 (2.8)
SN	1.3	1.6	2.0
CMB	3.0	1.7	2.5
SN + CMB	2.9	2.0	2.2
BAO + CMB	0.6	2.8	3.4
BAO + SN + CMB	1.2	1.8	**3.2**

This corresponds to the number of standard deviations that an event with the same probability would have had if it had been drawn from a Gaussian distribution.

In Table II, we present statistical deviations from ΛCDM for different datasets and some combination of them at each extension model considered in the analysis.

In interpreting these results, it is worth considering how this parameter shift metric differs from the primary model comparison statistics used in DES-SN5YR [8], which employs Bayesian evidence ratios, and in the DESI Y1 BAO analysis [20], which reports frequentist $\Delta\chi^2$ goodness-of-fit improvements. Compared to evidence ratios, our parameter shift metric is less directly sensitive to the choice of parameters' prior ranges; however, for weakly constrained posteriors, its reported significance may be impacted by how prior bounds (including in other parameter directions) shape the marginalized posteriors of the beyond-ΛCDM parameters. In the limit of Gaussian posteriors, the significance of deviations reported based on parameter shifts and $\Delta\chi^2$ is equivalent, as explored, e.g., in [75]. In contrast to parameter shifts, the value of $\Delta\chi^2$ is less sensitive to the prior and related projection effects, though it is subject to uncertainty due to noise in the χ^2-minimization procedure. Also, translating $\Delta\chi^2$ estimates to model comparison significances relies on assumptions of Gaussianity—both of the likelihood in data space and of the posterior in parameter space—which may not hold for all data combinations we consider.

Since these metrics provide complementary information, in Table III, we additionally report $\Delta\chi^2$ values for most of the same model and data combinations shown in Table II. (Data combinations with t_U are excluded because the method used to include that prior complicates the process of estimating χ^2.) For each combination, we estimate the minimum χ^2 by performing an ensemble of optimization searches launched from the 50 highest posterior samples from the associated chain. In parentheses, we also report the significance of these changes in goodness-of-fit using likelihood ratio tests and Wilks' theorem [76],[10] though we caution that for less constraining data combinations (less Gaussian posteriors) the focus should be put on the actual improvement of fit ($\Delta\chi^2$).

TABLE III. Improvement in goodness-of-fit from freeing additional model parameters computed via the difference between the minimum χ^2 estimated for ΛCDM and that for each extended model. Positive values indicate an improved fit in the extended model. Numbers in parentheses indicate the statistical significance in σs assuming a Gaussian approximation for the posterior, which may not be accurate for less constraining data combinations.

	$\Delta\chi^2$ improvement compared to ΛCDM		
Dataset	$k\Lambda$CDM	wCDM	w_0w_aCDM
BAO + SN + BBN	1.0 (1.0)	1.6 (1.3)	5.8 (1.9)
BAO + SN + $\theta_\star$	2.9 (1.7)	3.8 (2.0)	5.1 (1.8)
BAO+SN+$\theta_\star$+BBN	9.3 (3.1)	10.4 (3.2)	10.9 (2.9)
SN	1.0 (1.0)	1.6 (1.3)	5.9 (1.9)
CMB	8.9 (3.0)	3.3 (1.8)	4.2 (1.5)
SN + CMB	9.0 (3.0)	3.7 (1.9)	7.8 (2.3)
BAO + CMB	0.9 (0.9)	8.4 (2.9)	8.7 (2.5)
BAO + SN + CMB	1.6 (1.3)	3.5 (1.9)	**12.1**(**3.0**)

A common pattern in Table III is that for the most constraining combinations, there is a reasonable agreement on the significance of deviation to that reported in Table II (up to ∼0.5σ, well within the expected difference between methods; see [75]). As discussed above, for data combinations that are not particularly constraining, these methods are expected to differ, and both should be interpreted with caution. For most of the discussion in this paper, when quoting the significance of a deviation from ΛCDM, we will refer to the parameter shift metric of Table II, which is better suited for capturing non-Gaussian features of the posteriors.

2. Tensions among probes in a given model

To make sure that a deviation from the ΛCDM model is robust, we want to quantify the agreement of different probes within a given model before combining such datasets. To assess the consistency of parameter determinations from two posterior distributions, we calculate the probability of observing a parameter difference using the method

[10] We compute the probability to exceed our $\Delta\chi^2$ for a χ^2 PDF with the d.o.f. given by the number of beyond-ΛCDM parameters, and transform this via Eq. (21) to deviations in terms σ for a Gaussian PDF considering both tails.

TABLE IV. Tensions, in σs, among independent (combinations of) probes for a given model. See the methodology described in Sec. III C 2. For the case of t_U priors, we consider the fiducial Gaussian prior case and, in parenthesis, the case where only a lower bound on t_U is set. We note that these tensions are reported in the whole parameter space unlike deviations in Table II, which refer to the parameter additional to ΛCDM.

	Tension (σ)				
Datasets	ΛCDM	kΛCDM	wCDM	w_0w_aCDM	νΛCDM
BAO vs SN	0.5	0.0	0.0	0.3	0.2
CMB vs SN	1.7	1.5	1.3	1.1	1.2
CMB vs BAO	2.0	3.2	0.6	0.1	2.0
SN vs BAO + $\theta_\star$	2.4	...	...	...	...
CMB vs BAO + SN + BBN	2.2	3.3	2.2	1.2	...
SN vs BAO + BBN	0.4	...	...	...	...
SN vs BAO + BBN + $\theta_\star$	2.9	0.5	0.0	0.9	2.6
BAO + CMB vs SN	2.1	1.5	2.5	1.6	2.1
CMB vs BAO + SN + BBN + t_U	1.5 (0.8)	...	...	0.9 (0.9)	...

described in [73,74]. We start by building the posterior distribution of parameter differences. We consider each dataset, and in particular the two datasets denoted 1 and 2, to be independent. Under the assumption that the two-parameter sets that describe the datasets, $\mathbf{p}_1$, $\mathbf{p}_2$, differ, the joint distribution of their parameter determinations is given by the product of their posteriors,

$$P(\mathbf{p}_1, \mathbf{p}_2|d_1, d_2) = P_1(\mathbf{p}_1|d_1)P_2(\mathbf{p}_2|d_2). \qquad (22)$$

To compute the distribution of parameter differences, we change variables by defining $\Delta\mathbf{p} \equiv \mathbf{p}_1 - \mathbf{p}_2$, including all parameters shared by the two datasets. The distribution of $\Delta\mathbf{p}$ is obtained by marginalizing over one of the parameters,

$$P(\Delta\mathbf{p}) = \int P_1(\mathbf{p})P_2(\mathbf{p} - \Delta\mathbf{p})\mathrm{d}\mathbf{p}. \qquad (23)$$

The distribution of parameter differences, $P(\Delta\mathbf{p})$, provides insight into whether the parameter determinations from two datasets are consistent. Intuitively, if $P(\Delta\mathbf{p})$ has most of its support when $\Delta\mathbf{p}$ has large deviations from zero, the two parameter sets are incompatible, indicating a tension between the datasets. To quantify the probability of a parameter shift, we calculate the same integral as in Eq. (19) but for the parameter difference distribution defined in Eq. (23),

$$\Delta \equiv \int_{P(\Delta\mathbf{p})>P(0)} P(\Delta\mathbf{p})\mathrm{d}\Delta\mathbf{p}, \qquad (24)$$

which measures the posterior probability above the iso-density contour corresponding to no parameter shift ($\Delta\mathbf{p} = 0$). Since the distribution of parameter differences, $P(\Delta\mathbf{p})$, is an n-dimensional distribution, with n corresponding to the total number of parameters describing the assumed theoretical model, the integral in Eq. (24) is computationally more expensive to estimate than Eq. (19). For this reason, we use the machine-learning based method described in [73]. The first step is to train a normalizing flow on samples from $P(\Delta\mathbf{p})$, then we evaluate the tension integral as a Monte Carlo integral analogously to Eq. (20). We convert the probability of a shift into a number of standard deviations as in Eq. (21).

In Table IV, we show tension results for pairs of independent datasets in each cosmological model considered in this work.

IV. RESULTS

A. ΛCDM

We start by exploring constraints on the standard model, ΛCDM, in Figs. 2 and 3, where the latter shows a zoomed-in view of the region preferred by the CMB. For ΛCDM and all other models considered, we report the marginalized constraints on parameters in Table V, and additionally show H_0 and Ω_m constraints in Figs. 8 and 9, respectively.

One measurement of angular BAO on its own does not strongly constrain any individual parameter of the ΛCDM space, but it excludes parts of the parameter space [by combining Eqs. (2), (11), (12), and (13)]. Even if we add a BBN prior, the contours (not shown) do not close: we have two data points and three free parameters: Ω_m, Ω_b and H_0. Similarly, combining BAO + $\theta_\star$ is not sufficient to close the contours (not shown) in our prior volume, but offers us a measurement of $\Omega_\mathrm{m} = 0.255^{+0.021}_{-0.035}$. This bound is lower than that of CMB ($\Omega_\mathrm{m} = 0.3049^{+0.0082}_{-0.0090}$) and SN ($\Omega_\mathrm{m} = 0.353 \pm 0.017$), although we caution that it will be sensitive to the choice of prior on Ω_b and h since constraints on both of those parameters are degenerate with Ω_m and prior bounded.

Once we combine BAO with both BBN and $\theta_\star$, the contours close (dark green in Fig. 2), and we obtain competitive constraints, with $H_0 = 71.1 \pm 1.9\ \mathrm{km\,s^{-1}\,Mpc^{-1}}$ and $\Omega_\mathrm{m} = 0.263^{+0.020}_{-0.025}$. This is between the H_0 values from

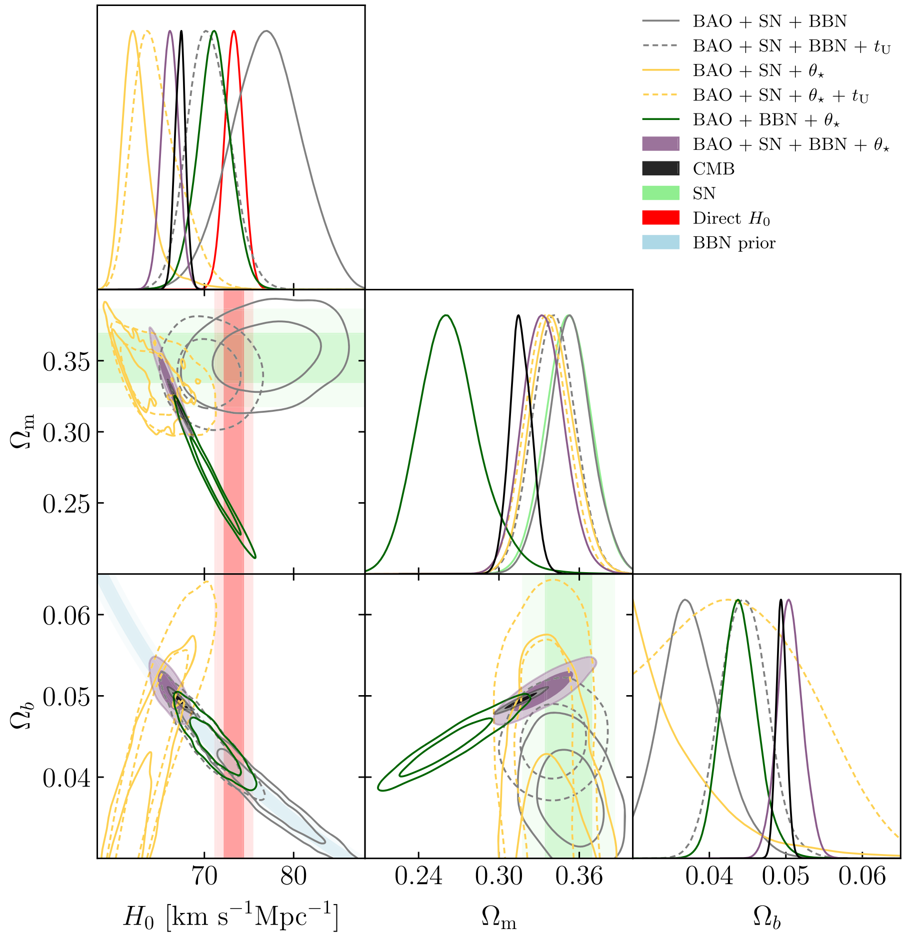

FIG. 2. **ΛCDM**. 68% (darker) and 95% (lighter) credible regions of the posteriors of different probe combinations within ΛCDM. Tensions between constraints are apparent. They are further discussed in the text and quantified in Table IV. We zoom in to the more constraining combinations (including CMB and BAO + SN + BBN + $\theta_\star$) in Fig. 3.

SH0ES and from *Planck*, and remains compatible with either measurement.

SN on its own tightly constrains matter abundance with a preference for high values, $\Omega_m = 0.353 \pm 0.017$. However, SN alone does not constrain H_0 unless their absolute magnitude is calibrated. One interesting way to perform that calibration is by combining BAO with information from the early Universe about r_d, e.g., from BBN, $\theta_\star$, or a CMB-based inference of r_d itself as we use in Sec. IV F. This allows us to use BAO to infer the distance to a given redshift [in our case, $D_M(z = 0.85)$], which calibrates the distance to supernovae. Fitting BAO + SN + $\theta_\star$ together results in a very low value of H_0, with $62.7^{+1.0}_{-2.1}$ km s^{-1} Mpc^{-1}. On the other hand, BAO + SN + BBN gives a high value of $H_0 = 76.9 \pm 3.9$ km s^{-1} Mpc^{-1}. If we combine all of these probes (BAO + SN + BBN + $\theta_\star$) we get $H_0 = 66.15 \pm 0.96$ km s^{-1} Mpc^{-1}, which is closer to *Planck*'s value (Table V). However, we discuss later in this section that some of these datasets are in some level of tension, and, hence, all these measurements should be taken with caution.

It is interesting to consider how these constraints change when we include the prior on the age of the Universe from globular clusters measurements in [56] (see Secs. II D and III B). We find that the t_U prior does not have any effect on posteriors when added to any inference including the CMB power spectra, since the CMB strongly constrains the age of the Universe. Similarly, it also had little impact when added to BAO + SN + BBN + $\theta_\star$, demonstrating that this data combination also bounds t_U and that those constraints agree with the added prior. However, t_U does add significant information when removing either BBN or $\theta_\star$. For BAO + SN + $\theta_\star$, adding t_U moves the contour away from the Ω_b prior edge by increasing its H_0 value. The contours are larger when including the t_U prior, but this is due to the BAO + SN + $\theta_\star$ case being artificially truncated by the lower bound of the Ω_b prior. In the case of BAO + SN + BBN, the t_U prior causes the contour to move to lower H_0 values and shrink. We note that the discrepancy between the H_0 values previously found between BAO + SN + BBN and BAO + BBN + $\theta_\star$ is reduced, but not completely ameliorated, when t_U is added to both data combinations.

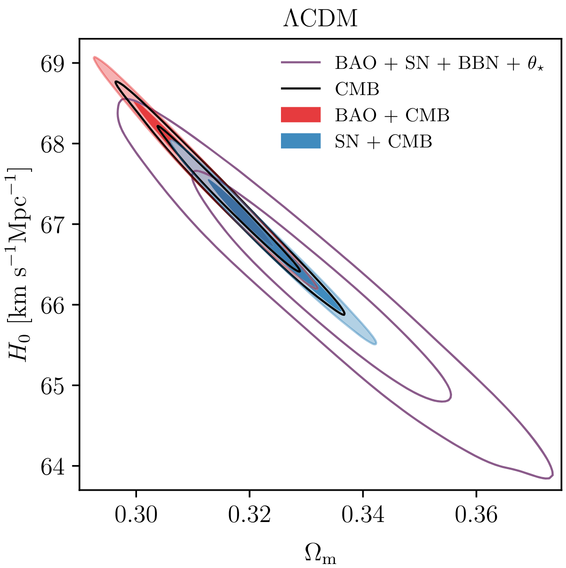

FIG. 3. **ΛCDM** zoom-in of the H_0-Ω_m plane to show the most constraining data combinations. We show the 68% and 95% credible regions of the posteriors. As we describe in Sec. IV A, BAO (red) and SN (blue) tend to push in different directions of the parameter space when combined with CMB. The background probe combination (purple) is in agreement with the CMB constraints besides coming from the combination of datasets in tension with CMB and/or among them, as discussed in the text.

The CMB measurements from *Planck* are very constraining in ΛCDM. Hence, even though BAO's D_M/r_d is $\sim 2\sigma$ below *Planck* 's prediction, when we combine BAO + CMB (red in Fig. 3). we only find a small shift in the cosmological parameters relative to *Planck* alone. Similarly, if we add SN to CMB, the shift is small. However, it is noticeable in Fig. 3 that the different Ω_m values preferred by BAO and SN push the combined constraints in opposite directions.

In Table IV, we check the consistency of different probes with the methodology from [73], summarized in Sec. III C. We find a mild-low level of tension between CMB and either SN (1.7σ) or BAO (2.0σ). Whereas BAO and SN seem very compatible, we find that the combination of BAO + $\theta_\star$ is in tension (2.4σ) with SN. This was already hinted by Fig. 2 and has implications for the interpretation of differences between H_0 constraints from BAO + SN + BBN versus BAO + SN + $\theta_\star$: the latter comes from a combination of datasets in tension, and so is a less trustworthy inference. The fact that BAO + SN + $\theta_\star$ hits the bounds of the (wide) Ω_b prior range can also be seen as an indication that this combination did not work well in ΛCDM. We also find the BAO + SN + BBN combination to be in tension with CMB (2.2σ); however, this tension is alleviated when the t_U prior is added to the former (1.5σ, see Table IV).

In conclusion, we find a number of tensions between datasets in ΛCDM. From D_M/r_d comparisons in our previous DES BAO analysis [6], CMB and BAO are known to have some level of discrepancy in ΛCDM. If we isolate just the geometric information from the CMB measurement of $\theta_\star$ and combine it with BAO, then this dataset becomes discrepant with SN. On the other hand, the BAO + SN + BBN combination is also in tension with CMB, but pulling in the opposite direction of H_0 to BAO + SN + $\theta_\star$. When adding t_U priors, both BAO + SN + $\theta_\star$ and BAO + SN + BBN come closer both to each other and to the CMB inferences, reducing some of the tensions. Besides those relative tensions, we note that the combination BAO + SN + BBN + $\theta_\star$ coming from combinations of datasets in tension) is compatible with the CMB constraints, and in agreement with t_U priors. Finally, BAO tends to favor lower values of Ω_m, but SN prefers higher values of Ω_m. All of these discrepancies in ΛCDM provide an interesting context for our explorations of extended cosmological models.

B. *k*ΛCDM

A natural extension of the ΛCDM model is *k*ΛCDM, in which we allow curvature to vary. Results for our *k*ΛCDM analysis are shown in Fig. 4 and the second block of Table V. It is well known that constraints from the CMB alone exhibit a strong geometric degeneracy between Ω_k and Ω_m [53], which translates to a degeneracy between Ω_m and $\Omega_\Lambda = 1 - \Omega_m - \Omega_k$ in Fig. 4. From the CMB alone, we find $\Omega_k = -23.6^{+4.2}_{-7.9} \times 10^{-3}$, in $\sim 3\sigma$ tension with flatness according to the model-comparison metric described in Sec. III C 1 and reported in Table II. This is consistent with previous findings that have been extensively discussed in the literature (e.g., [17,53,77–80]).

If we add BAO to CMB, we recover $\Omega_k = 1.4^{+5.8}_{-4.0} \times 10^{-3}$, compatible with flat-ΛCDM. On the other hand, if we add SN to CMB, the constraints are in tension with flatness at a 2.9σ significance, on the negative side of $\Omega_k = -14.2^{+5.3}_{-4.9} \times 10^{-3}$.[11] When BAO + SN + CMB are all combined, we find $\Omega_k = -5.5^{+4.6}_{-4.2} \times 10^{-3}$, within $\sim 1\sigma$ of flat-ΛCDM, though the fact that BAO + CMB and SN + CMB prefer different values of Ω_k by $\sim 3\sigma$ means this combined result should be interpreted with caution.

If we consider a purely background data combination of CMB's $\theta_\star$ with BAO and SN, we obtain $\Omega_k = 45^{+18}_{-14} \times 10^{-3}$, again, mildly away from flatness ($\sim 2.5\sigma$, see Table II), but on the $\Omega_k > 0$ side. Similar and tighter results are recovered when we add BBN, with BAO + SN + BBN + $\theta_\star$ shown in purple in Fig. 4, giving $\Omega_k = 45^{+15}_{-14} \times 10^{-3}$, 2.8σ from flatness.

Looking individually at each dataset, SN constrains one direction in the Ω_m-Ω_Λ plane relatively well. In our setup,

[11]Note, as discussed in Sec. II C, that the CMB implementation used here is different to that in the DES SN paper [8], where we found $\Omega_k = (-10 \pm 5) \times 10^{-3}$ for CMB + SN. We also note that in earlier versions of [8] there was a typo in the sign of this constraint.

TABLE V. We report the 68% credible region (1σ) or 95% of the upper/lower limit of cosmological parameters (in columns) under different cosmological models (in five tiers) and different data combinations. See the methodology in Sec. III B. H_0 is given in units of $\mathrm{km\,s^{-1}\,Mpc^{-1}}$ and neutrino mass in eV. We highlight in bold what we consider our main constraints.

	H_0	$\Omega_{\rm m}$	$\Omega_{\rm b}$	$10^3\Omega_k$	w_0	w_a	$\sum m_\nu$
			ΛCDM				
SN	⋯	0.353 ± 0.017	⋯	⋯	⋯	⋯	⋯
BAO + SN + BBN	76.9 ± 3.9	0.353 ± 0.016	<0.045	⋯	⋯	⋯	⋯
BAO + SN + BBN + $t_{\rm U}$	$70.5^{+2.2}_{-2.5}$	$0.341^{+0.015}_{-0.016}$	0.0445 ± 0.0030	⋯	⋯	⋯	⋯
BAO + $\theta_\star$	>64.4	$0.255^{+0.021}_{-0.035}$	$0.050^{+0.014}_{-0.008}$	⋯	⋯	⋯	⋯
BAO + SN + $\theta_\star$	$62.7^{+1.0}_{-2.1}$	$0.340^{+0.015}_{-0.017}$	<0.052	⋯	⋯	⋯	⋯
BAO + SN + $\theta_\star$ + $t_{\rm U}$	$64.7^{+1.8}_{-3.1}$	0.335 ± 0.016	<0.059	⋯	⋯	⋯	⋯
BAO + BBN + $\theta_\star$	71.1 ± 1.9	$0.263^{+0.020}_{-0.025}$	$0.0440^{+0.0021}_{-0.0025}$	⋯	⋯	⋯	⋯
BAO + SN + BBN + $\theta_\star$	66.15 ± 0.96	$0.333^{+0.015}_{-0.016}$	$0.0506^{+0.0015}_{-0.0017}$	⋯	⋯	⋯	⋯
SH0ES	73.04 ± 1.04	⋯	⋯	⋯	⋯	⋯	⋯
CMB	$67.30^{+0.57}_{-0.61}$	$0.3163^{+0.0084}_{-0.0080}$	$0.0494^{+0.0007}_{-0.0007}$	⋯	⋯	⋯	⋯
BAO + CMB	$67.62^{+0.59}_{-0.59}$	$0.3118^{+0.0080}_{-0.0082}$	$0.0490^{+0.0007}_{-0.0007}$	⋯	⋯	⋯	⋯
SN + CMB	$66.74^{+0.54}_{-0.55}$	$0.3242^{+0.0079}_{-0.0076}$	$0.0500^{+0.0007}_{-0.0006}$	⋯	⋯	⋯	⋯
BAO + SN + CMB	$67.03^{+0.53}_{-0.55}$	$0.3200^{+0.0074}_{-0.0079}$	$0.0497^{+0.0006}_{-0.0006}$	⋯	⋯	⋯	⋯
			***k*ΛCDM**				
SN	⋯	$0.317^{+0.032}_{-0.052}$	–	>-100	⋯	⋯	⋯
BAO + SN + $\theta_\star$	>65.9	$0.336^{+0.014}_{-0.015}$	$0.043^{+0.007}_{-0.008}$	45^{+18}_{-14}	⋯	⋯	⋯
BAO + SN + BBN + $\theta_\star$	$74.75^{+3.1}_{-3.0}$	$0.337^{+0.014}_{-0.015}$	$0.0400^{+0.0030}_{-0.0036}$	45^{+15}_{-14}	⋯	⋯	⋯
CMB	<63.5	$0.408^{+0.031}_{-0.017}$	>0.0563	$-23.6^{+4.2}_{-7.9}$	⋯	⋯	⋯
BAO + CMB	$68.3^{+2.5}_{-2.1}$	$0.307^{+0.017}_{-0.024}$	$0.0482^{+0.0027}_{-0.0038}$	$1.4^{+5.8}_{-4.0}$	⋯	⋯	⋯
SN + CMB	62.1 ± 1.6	$0.369^{+0.018}_{-0.018}$	$0.0585^{+0.0030}_{-0.0032}$	$-14.2^{+5.3}_{-4.9}$	⋯	⋯	⋯
BAO + SN + CMB	65.1 ± 1.6	$0.338^{+0.015}_{-0.017}$	$0.0530^{+0.0026}_{-0.0029}$	$-5.5^{+4.6}_{-4.2}$	⋯	⋯	⋯
			***w*CDM**				
SN	⋯	$0.264^{+0.081}_{-0.065}$	–	⋯	$-0.82^{+0.15}_{-0.11}$	⋯	⋯
BAO + SN + BBN	<81.5	$0.283^{+0.067}_{-0.059}$	$0.049^{+0.0087}_{-0.013}$	⋯	$-0.85^{+0.15}_{-0.10}$	⋯	⋯
BAO + SN + $\theta_\star$	$68.9^{+4.6}_{-6.6}$	$0.278^{+0.023}_{-0.029}$	>0.030	⋯	$-0.826^{+0.062}_{-0.047}$	⋯	⋯
BAO + SN + BBN + $\theta_\star$	67.0 ± 1.0	$0.281^{+0.018}_{-0.020}$	0.0495 ± 0.0016	⋯	$-0.828^{+0.049}_{-0.043}$	⋯	⋯
CMB	>65.1	$0.244^{+0.016}_{-0.052}$	<0.0520	⋯	$-1.32^{+0.12}_{-0.25}$	⋯	⋯
BAO + CMB	>72.0	$0.223^{+0.011}_{-0.031}$	<0.0427	⋯	$-1.41^{+0.08}_{-0.17}$	⋯	⋯
SN + CMB	$65.66^{+0.76}_{-0.75}$	$0.3326^{+0.0086}_{-0.0088}$	$0.0519^{+0.0012}_{-0.0012}$	⋯	-0.946 ± 0.028	⋯	⋯
BAO + SN + CMB	$65.97^{+0.79}_{-0.77}$	$0.3282^{+0.0090}_{-0.0092}$	0.0515 ± 0.0012	⋯	$-0.948^{+0.028}_{-0.027}$	⋯	⋯
			$w_0 w_a$CDM				
SN	⋯	$0.377^{+0.066}_{-0.022}$	⋯	⋯	$-0.82^{+0.13}_{-0.11}$	<0.18	⋯
BAO + SN + BBN	>62.8	$0.362^{+0.062}_{-0.025}$	<0.055	⋯	$-0.79^{+0.12}_{-0.10}$	<0.11	⋯
BAO + SN + BBN + $t_{\rm U}$	$69.6^{+2.4}_{-2.5}$	$0.308^{+0.029}_{-0.036}$	0.0460 ± 0.0034	⋯	-0.76 ± 0.11	$-0.79^{+0.87}_{-0.67}$	⋯
BAO + SN + $\theta_\star$	<79.6	$0.298^{+0.029}_{-0.037}$	–	⋯	-0.74 ± 0.10	$-0.76^{+0.86}_{-0.61}$	⋯
BAO + SN + $\theta_\star$ + $t_{\rm U}$	$68.4^{+3.1}_{-3.3}$	$0.293^{+0.024}_{-0.031}$	$0.0502^{+0.0091}_{-0.0076}$	⋯	$-0.74^{+0.09}_{-0.10}$	$-0.72^{+0.82}_{-0.58}$	⋯
BAO + SN + BBN + $\theta_\star$	67.5 ± 1.2	$0.295^{+0.020}_{-0.025}$	0.0487 ± 0.0018	⋯	$-0.74^{+0.09}_{-0.10}$	$-0.72^{+0.77}_{-0.55}$	⋯
BAO + SN + BBN + $\theta_\star$ + $t_{\rm U}$	$67.8^{+1.1}_{-1.2}$	$0.296^{+0.020}_{-0.025}$	$0.0486^{+0.0017}_{-0.0019}$	⋯	$-0.74^{+0.09}_{-0.10}$	$-0.78^{+0.75}_{-0.54}$	⋯
CMB	>65.4	$0.247^{+0.040}_{-0.056}$	<0.0518	⋯	>-1.6	<0.52	⋯
BAO + CMB	>67.1	$0.242^{+0.019}_{-0.050}$	<0.0488	⋯	>-1.5	<0.089	⋯
SN + CMB	67.3 ± 1.0	$0.317^{+0.010}_{-0.011}$	$0.0495^{+0.0013}_{-0.0015}$	⋯	-0.73 ± 0.11	$-1.09^{+0.57}_{-0.51}$	⋯
BAO + SN + CMB	$\mathbf{67.81^{+0.96}_{-0.86}}$	$\mathbf{0.3109^{+0.0086}_{-0.0099}}$	$\mathbf{0.0488^{+0.0012}_{-0.0014}}$	⋯	$\mathbf{-0.673^{+0.098}_{-0.097}}$	$\mathbf{-1.37^{+0.51}_{-0.50}}$	⋯
			νΛCDM				
CMB	$66.9^{+1.3}_{-0.7}$	$0.321^{+0.009}_{-0.017}$	$0.0499^{+0.0008}_{-0.0017}$	⋯	⋯	⋯	<0.28
BAO + CMB	$67.70^{+0.80}_{-0.64}$	$0.311^{+0.008}_{-0.011}$	$0.0489^{+0.0007}_{-0.0010}$	⋯	⋯	⋯	<0.15
SN + CMB	$65.8^{+1.1}_{-0.9}$	$0.336^{+0.012}_{-0.016}$	$0.0514^{+0.0012}_{-0.0018}$	⋯	⋯	⋯	<0.37
BAO + SN + CMB	$66.66^{+0.96}_{-0.72}$	$0.325^{+0.009}_{-0.013}$	$0.0503^{+0.0009}_{-0.0014}$	⋯	⋯	⋯	<0.27

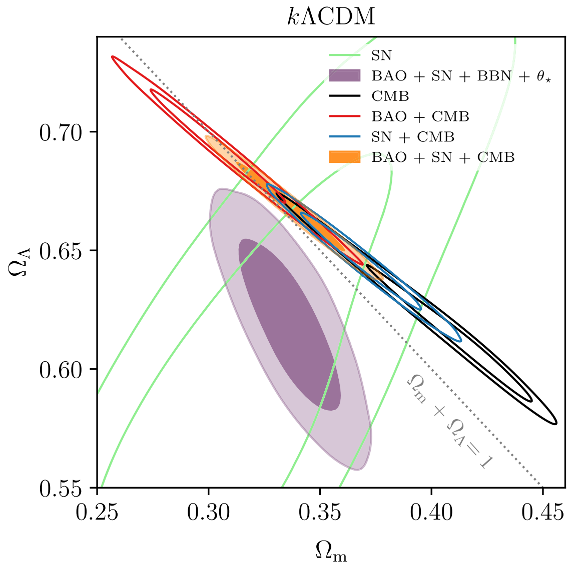

FIG. 4. ***k*ΛCDM**. 1 and 2σ contours of the 2D posterior of Ω_m and $\Omega_\Lambda \equiv (1 - \Omega_k - \Omega_\mathrm{m})$ in $k\Lambda$CDM. The tension among probes in this model is manifest. BAO + CMB and SN + CMB differ by $\sim 3\sigma$ in Ω_k and the background probe combination (purple) is in tension with the CMB constraints. See Sec. IV B for discussion.

the posterior on Ω_k hits the upper side of our prior ($\Omega_k = 0.25$), but if that prior was wider, as it is in [8], the contours would eventually close. BAO, although not shown here, disfavors the upper-right part of Fig. 4. These two probes intersect the CMB at different points along its Ω_Λ-Ω_m degeneracy direction. Table IV shows that the tensions between CMB and either BAO and SN do not decrease by varying curvature. Interestingly, while in $k\Lambda$CDM, we find that the tension between SN and BAO + BBN + $\theta_\star$ goes away (Table IV), in Fig. 4 we find that the background-only constraints (BAO + SN + BBN + $\theta_\star$) are now discrepant with constraints based on CMB power spectra.

In summary, in $k\Lambda$CDM we do not find a general alleviation of the tensions among the probes, and some tensions actually increase. Additionally, BAO + SN + BBN + $\theta_\star$ and BAO + SN + CMB give very different posteriors on Ω_k. We, therefore, conclude that adding curvature to our model does not relieve the difficulty in reconciling constraints from the different observables we consider.

C. *w*CDM

Next, we consider a one-parameter extension of ΛCDM in which we constrain a constant equation of state of dark energy w. We present these wCDM results in Fig. 5.

As in $k\Lambda$CDM, the CMB has difficulties constraining this additional parameter on its own. Nevertheless, it gives a (wide) bound of $w = -1.32^{+0.12}_{-0.25}$, at 1.7$\sigma$ from ΛCDM ($w = -1$), again with that deviation's significance evaluated using the method from Sec. III C 1 and reported in Table II. If we add BAO to CMB, the contours tighten to $w = -1.41^{+0.08}_{-0.17}$, resulting in a 2.8$\sigma$ deviation from ΛCDM. Such a deviation from ΛCDM is not unexpected, as we recall that the BAO D_M/r_d constraint is $\sim 2\sigma$ away from the CMB-ΛCDM prediction. Compared to ΛCDM, the tension between the CMB and BAO measurements reduces in significance from 2.0σ to 0.6σ (see Table IV), i.e., effectively removing the tension.

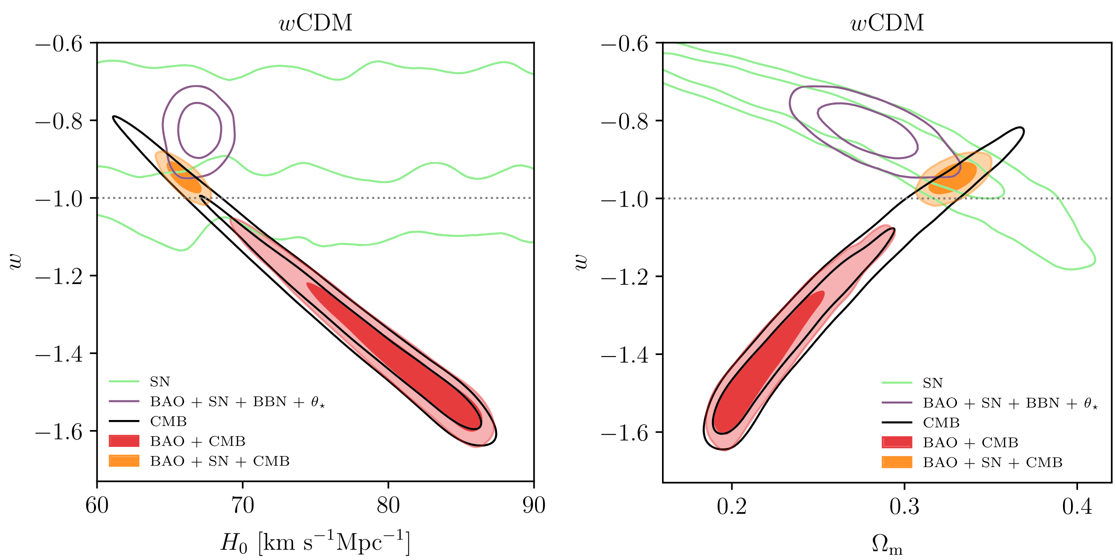

FIG. 5. ***w*CDM**. 1 and 2σ contours of the 2D posterior of w-H_0 (left) and w-Ω_m (right). BAO and SN still push for different regions of parameter space, $w < -1$ and $w > -1$, respectively. Nevertheless, SN dominates the constraints on w. Some tensions among probes are still apparent, as discussed in Sec. IV C.

SN on its own prefers a higher-than-standard value of the equation of state $w = -0.82^{+0.15}_{-0.11}$, which is $\sim 1.6\sigma$ away from ΛCDM. If we combine SN + CMB results we obtain $w = -0.946 \pm 0.028$, obtaining a ∼3% precision in w and a 2.0σ deviation from ΛCDM. Adding BAO to that barely changes the results, giving $w = -0.948^{+0.028}_{-0.027}$ and slightly decreasing the deviation ΛCDM to 1.8σ, though we caution that the combination of BAO + CMB is in 2.5σ tension with SN. An interesting feature is that whereas SN and CMB have a large degeneracy in the $\{w, \Omega_{\rm m}\}$ plane (right panel of Fig. 5), they overlap relatively close to the ΛCDM value ($w = -1$).

Background-only constraints on w are largely driven by the SN measurements. Like SN-alone, the background combination of BAO + SN + $\theta_\star$ prefers $w > -1$ at a significance of 2.7σ ($w = -0.826^{+0.062}_{-0.047}$), increasing to 3.1σ when adding BBN ($w = -0.828^{+0.049}_{-0.043}$). The non-CMB combination of BAO + SN + BBN also prefers this region ($w = -0.85^{+0.15}_{-0.10}$), but with small significance (1.4σ). All of these combinations give relatively similar w constraints to SN alone, but the added observables additionally allow us to constrain the Hubble constant. The combination of all the background constraints (BAO + SN + BBN + $\theta_\star$) results in $H_0 = 67.0 \pm 1.0$ km s^{-1} Mpc^{-1} and $\Omega_{\rm m} = 0.337^{+0.014}_{-0.015}$, much tighter constraints than the SN-only value of $\Omega_{\rm m} = 0.264^{+0.081}_{-0.065}$. It is also worth noting that extending to wCDM fully alleviates the tension seen in ΛCDM between SN and BAO + BBN + $\theta_\star$.

To sum up, as we have seen for other models, BAO and SN tend to pull constraints in different directions of the wCDM parameter space. While extending to wCDM reduces some tensions—between CMB and BAO, as well as between SN and BAO + BBN + $\theta_\star$—it does not reconcile all of our observables. Notably, when combined with the CMB, non-negligible tensions remain between BAO and SN inferences. Since BAO and SN probe different redshifts, this motivates extending the model further with a time-dependent equation of state for dark energy.

D. $w_0 w_a$CDM

Constraints on $w_0 w_a$CDM are shown in Fig. 6. On the left, we show results from the CMB alone, which is not strongly constraining this parameter space and finds a 2.5σ deviation from the ΛCDM case (as always, quantified using the method described in Sec. III C and reported in Table II). Adding BAO pushes the contours to lower values of w_a, resulting in a 3.4σ tension with ΛCDM, but do not dramatically change the constraints. In the right panel of Fig. 6, we see that SN on their own can give two-sided constraints on w_0 well within our priors. Whereas SN can also give two-sided constraints on w_a if one chooses broad priors (with the 1-σ bound reaching $w_a \sim -15$, see [8]), the constraints hit our lower limit described in Table I. When combining SN with CMB, the contours close well within our priors in the $w_0 - w_a$ plane (shown in the left panel) and leave a 2.2σ deviation from ΛCDM.

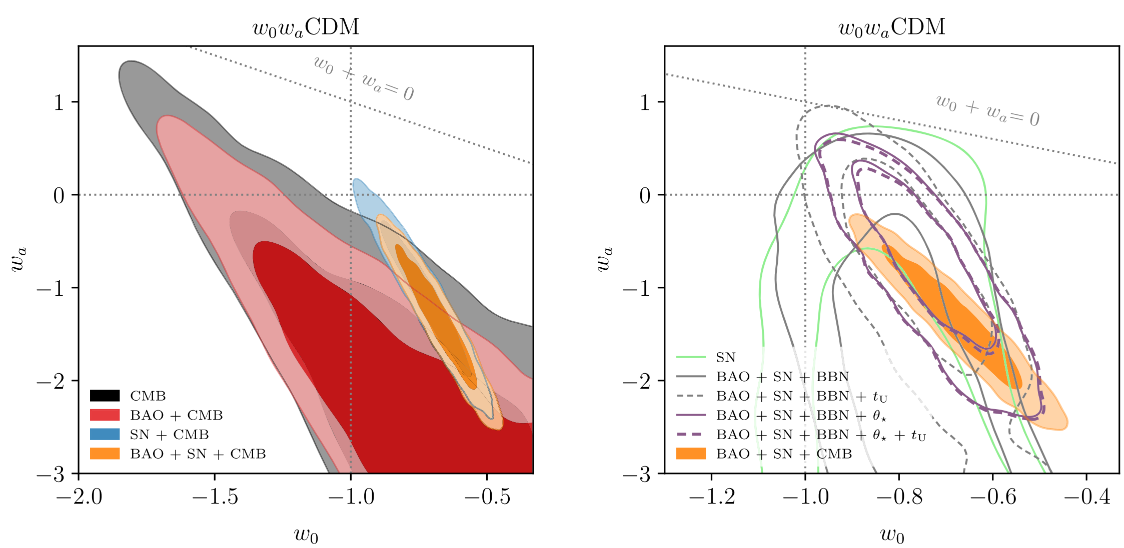

FIG. 6. Constraints on the $\boldsymbol{w_0 w_a}$**CDM** model. Left: Constraints from the CMB and its combinations with SN and BAO, with our main constraint, BAO + SN + CMB, in orange. Right: We zoom-in and compare the main constraint from BAO + SN + CMB (orange) to other inferences that do not rely on CMB power spectra. All probes tend to prefer the lower-right (high w_0, low w_a) quadrant and tensions between different observables are much relaxed relative to ΛCDM (see Table IV). Our main constraint, BAO + SN + CMB (orange), disfavors ΛCDM ($w_0 = -1$, $w_a = 0$) at a 3.2σ significance (Table II). The background-only (dashed-purple) and non-CMB (dashed-gray) cases also show 2.8σ and 2.0σ deviations from ΛCDM, respectively. See Sec. IV D for more details and discussion. The gray-dotted line indicate the ΛCDM case ($w_0 = -1$, $w_a = 0$), and the limit of the $w_0 + w_a < 0$ prior.

When we add BAO to SN and CMB, the contours shrink slightly and move towards lower values of w_a, resulting in a 3.2σ deviation from ΛCDM and

$$\left.\begin{aligned} w_0 &= -0.673^{+0.098}_{-0.097} \\ w_a &= -1.37^{+0.51}_{-0.50} \end{aligned}\right\}\mathrm{BAO} + \mathrm{SN} + \mathrm{CMB}. \quad (25)$$

On the right-hand side of Fig. 6, we compare the tightest constraint (BAO + SN + CMB, in orange in both panels) to other data combinations that do not rely on the CMB power spectra. Compared to SN alone, the CMB-independent combination of BAO + SN + BBN gives similar constraints on w_0-w_a.

To further characterize these results, we now consider adding a prior on the age of the Universe, t_U, as described in Sec. II D. Most notably, adding this prior to BAO + SN + BBN has a large impact, as seen in the comparison between solid and dashed gray lines in the right panel of Fig. 6. We find

$$\left.\begin{aligned} w_0 &= -0.76 \pm 0.11 \\ w_a &= -0.79^{+0.87}_{-0.67} \end{aligned}\right\}\mathrm{BAO} + \mathrm{SN} + \mathrm{BBN} + t_\mathrm{U}. \quad (26)$$

In contrast to the BAO + SN + BBN constraint, BAO + SN + BBN + t_U produces closed contours in both w_0 and w_a, fully independent of the CMB (which did not provide close contours on its own). This case is 2σ away from ΛCDM. Another interesting case is when we also add $\theta_\star$ from the CMB to obtain our tightest constraint from the background expansion probes alone,

$$\left.\begin{aligned} w_0 &= -0.74^{+0.09}_{-0.10} \\ w_a &= -0.78^{+0.75}_{-0.54} \end{aligned}\right\}\mathrm{BAO} + \mathrm{SN} + \mathrm{BBN} + \theta_\star + t_\mathrm{U}. \quad (27)$$

We find that once $\theta_\star$ is added to BAO + SN (with or without BBN), the t_U prior does not add much information. Hence, we conclude that BAO + SN + $\theta_\star$ already determines the age of the Universe and that determination agrees with the t_U prior we are considering.

Whereas in ΛCDM and one-parameter extensions discussed above, we find that SN and BAO tend to push parameter constraints in different directions, this is not the case in w_0w_aCDM. This is partially due to the model's increased flexibility since BAO moves mostly w_a and SN mostly constraints w_0, as can be seen in the left and right panels of Fig. 6, respectively. Regarding the tension metrics reported in Table IV, we find that the tension between CMB and BAO seen in ΛCDM is completely alleviated (0.1σ for w_0w_aCDM versus 2.0σ for ΛCDM), and other tension metrics, e.g., between SN and either the CMB or BAO + CMB, are also reduced. These tension metrics indicate that all the data combinations we consider agree within this model. This observation is reinforced by the fact that their 1-σ confidence regions overlap in the lower-right quadrant of the w_a vs w_0 plane. We also remark that, even though we impose a $w_0 + w_a < 0$ prior (see Sec. III B), this region of space is also naturally excluded by the data, since none of the data combinations highlighted (except, marginally, BAO + SN + BBN + t_U) hit this prior within the 2σ contours.

Our tightest constraint, BAO + SN + CMB, disfavors ΛCDM at 3.2σ significance. It is remarkable that this is at a comparable level of significance to the recent results reported by DESI [20] from their combined analysis of *Planck* CMB, DES SN, and DESI 2024 BAO. To more directly compare, in Appendix A, we reanalyze the DESI BAO results using our analysis framework and priors, finding the deviation from ΛCDM to be 3.6σ when combining SN + CMB + DESI2024BAO.[12] The combination of DESI BAO with DES BAO, DES SN and CMB could show an even higher deviation from ΛCDM, as discussed in Appendix A.

E. νΛCDM

Another interesting extension[13] of ΛCDM is the variation of neutrino mass. Whereas in all analyses described above we fixed the sum of neutrino masses to $\sum m_\nu = 0.06$ eV, we now let it vary as described in Sec. III A, below Eq. (11). We focus on constraints including CMB measurements, shown in Fig. 7. The fact that the CMB primarily constrains CDM and baryon densities produces the degeneracy between $\sum m_\nu$ and Ω_m seen for all contours.

Variations between different data combinations can thus be interpreted in terms of how that degeneracy is broken via constraints on Ω_m. The CMB on its own only places a 95% upper limit of $\sum m_\nu < 0.28$ eV, with the Ω_m information coming largely from the damping produced by lensing on the high-ℓ power spectra. As BAO prefers a lower value of Ω_m than CMB, the BAO + CMB combination pushes that bound down to $\sum m_\nu < 0.15$ eV. On the other hand, because SN prefers a high value of Ω_m, SN + CMB relaxes the limit on neutrino mass to $\sum m_\nu < 0.37$ eV. If we combine all of BAO + SN + CMB, we obtain $\sum m_\nu < 0.27$ eV. These results, with BAO tightening $\sum m_\nu$ constraints compared to the CMB alone and DES SN tending to weaken them, are in line with what has been previously seen in the DESI BAO analysis [20] as well as [63]. We note that our BAO + CMB neutrino mass bounds are higher than those reported for DESI BAO

[12] The deviations quoted here differ slightly from those quoted in [20] and those in [24], as those papers adopt a the method based on $\Delta\chi^2$, whereas we quantify deviation in terms of parameter shifts (see Sec. III C 1). We also use only temperature and polarization from CMB; see Sec. II C.

[13] One could argue that neutrinos are known to have mass, and hence, this should not be considered an extension. For example, in DES 3 × 2pt neutrino masses are always varied in the baseline analysis [16].

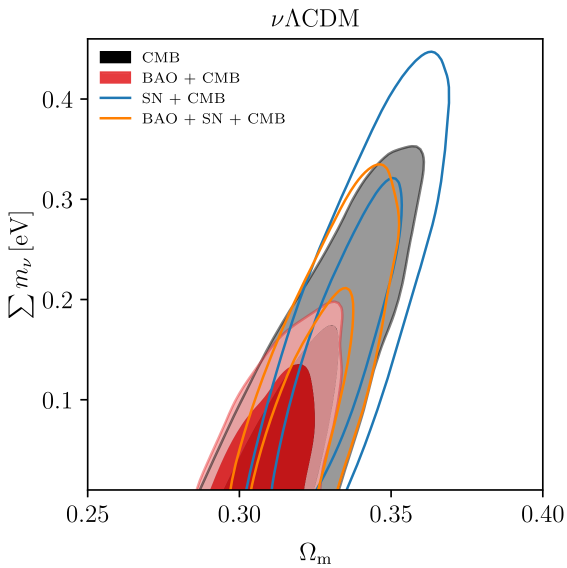

FIG. 7. **$\nu\Lambda$CDM**. 1 and 2σ contours of the posterior of the neutrino mass vs matter density. Given the degeneracy of these two parameters set by CMB, the preference for high-Ω_m by SN results in a relaxation of the $\sum m_\nu$ bounds, while the low-Ω_m preference by BAO translates to tighter constraints.

(0.072 eV), reflecting the fact that DES BAO Ω_m constraints are weaker and compatible with higher values than those from DESI BAO. As discussed for DESI BAO and other BAO studies in the literature (e.g., [20,81,82]), our BAO + CMB bounds are tight enough that the peak of the marginalized posterior hits the lower $\sum m_\nu = 0$ prior bound and would peak at $\sum m_\nu < 0$ if one were to fit that posterior with a Gaussian that allowed negative values. In contrast, the peak of the marginalized posteriors for SN + CMB occurs at $\sum m_\nu > 0$.

Finally, we remark that according to Table IV, freeing the neutrino masses does not alleviate significantly the tensions among probes.

F. Cosmographic expansion

Next, we use a cosmographic expansion [83,84] to measure H_0 using the DES BAO + SN with an external calibration of the sound horizon, r_d. A cosmographic expansion is a Taylor expansion of the scale factor a that is agnostic about the energy contents of the Universe while maintaining the assumptions of homogeneity and isotropy. We follow the same definitions and methodology defined in Sec. 2 of [67], which assumes a spatially flat Universe. We determine our result using the fourth order expansion and a Gaussian prior on the sound horizon from [54] of $r_d \sim \mathcal{N}(147.46, 0.28)$ Mpc (see Sec. II C 3). We obtain

$$H_0 = 68.6^{+1.7}_{-1.6}\ \mathrm{km\,s^{-1}\,Mpc^{-1}}, \tag{28}$$

which is consistent with the *Planck* ΛCDM value along with previous inverse distance ladder measurements [67,85,86].

We use the Akaike information criterion, $\mathrm{AIC} \equiv 2k - 2\ln\mathcal{L}^{\max}$ [87], where k is the number of parameters in the model, to assess whether the additional parameters used in the higher order cosmographic models are required by the data. We find the fourth order cosmographic model used to obtain our key result quoted above, to have a strong and moderate preference over the second and third order models, respectively. However, we find no preference for or against the fourth and fifth order expansions and therefore, focus on the model with fewer parameters.

G. Comparison of H_0 & Ω_m across models

In this section, we compare the values of Ω_m and H_0 inferred from all relevant combinations of models and probes. We summarize these results in Fig. 8, which shows 68% c.r. H_0 constraints, and Fig. 9, which shows 68% c.r. Ω_m constraints. As a reference for the H_0 constraints, Fig. 8 shows a band with the direct-H_0 (SH0ES) results in red and the *Planck* -ΛCDM results in black, highlighting the known tension between those measurements. For Ω_m constraints in Fig. 9, we show two bands corresponding to the 1-σ intervals for CMB (black) and SN (light green) in ΛCDM, whose tension is quantified as 1.7σ (Table IV).

We remind the reader that CMB tend to constrain the combination $\Omega_m {H_0}^2$ very well. Hence, Ω_m and H_0 measurements typically anti-correlate. Particularly, SN or BAO do not constrain H_0 on their own, but their constraints on Ω_m propagate to H_0 when combining them with CMB thanks to that degeneracy. With this in mind, we focus our discussion below on the Hubble constant, but similar effects (in the opposite direction) can be seen in Ω_m. We note the following highlights:

(i) Within ΛCDM, BAO tends to push H_0 CMB constraints to slightly higher values, whereas SN tends to push for lower values of H_0 (via the $\Omega_m - H_0$ anticorrelation imposed by CMB). However, the constraining power of the CMB dominates when combined with SN and/or BAO.

(ii) In ΛCDM, we can obtain H_0 constraints from only BAO + BBN + $\theta_\star$. These bounds fall between those from *Planck* and SH0ES but are closer to the latter.

(iii) In ΛCDM, very low values of H_0 are obtained with BAO + SN + $\theta_\star$. However, these inferences are driven by tensions between SN and BAO + $\theta_\star$, with the latter preferring extreme values for Ω_b (hitting our priors) and the age of the Universe. Hence, this tension relaxes when including BBN and/or t_U priors, bringing the H_0 values up.

(iv) BAO pushes to higher values of H_0 when added to CMB in all models considered. This is particularly significant for wCDM, where BAO + CMB places a lower bound on H_0 that is consistent with the value from SH0ES and not with *Planck* -alone. However, we note this combination (BAO + CMB for wCDM)

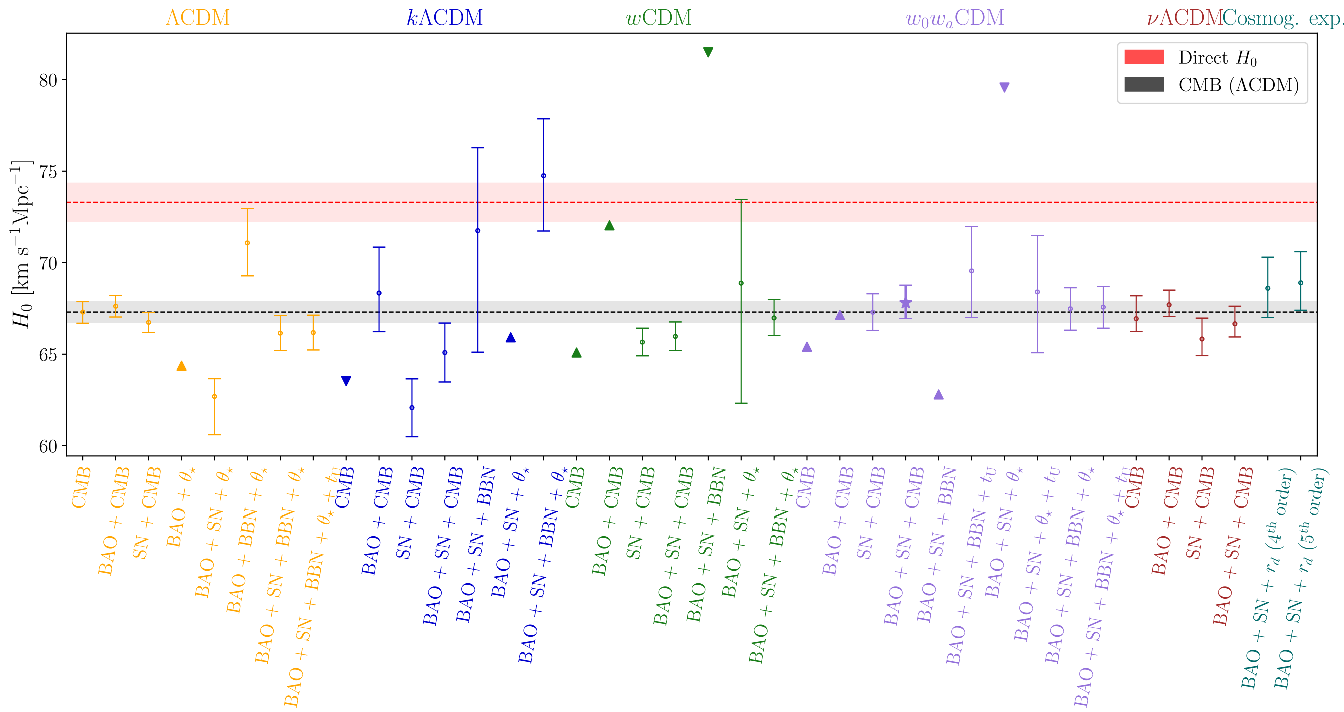

FIG. 8. Hubble constant constraints for most of the combinations of models and datasets considered in this work, visualizing values reported in Table V. Two-sided 1-σ (68% c.r.) constraints are shown as points with error bars, and one-sided 95% upper/lower limits are shown as triangular markers with the point facing down/up. We also show the SH0ES and the CMB-ΛCDM constraints as shaded bands for comparison. We note that H_0 anti-correlates with $\Omega_{\rm m}$ (shown in Fig. 9) when including CMB with other probe combinations. Besides the variety of values, we note that the more extreme constraints are associated with tensions between datasets and that our main results (BAO + SN + CMB in w_0w_aCDM, marked with a star) agree with CMB-ΛCDM (gray band). See discussion in Sec. IV G.

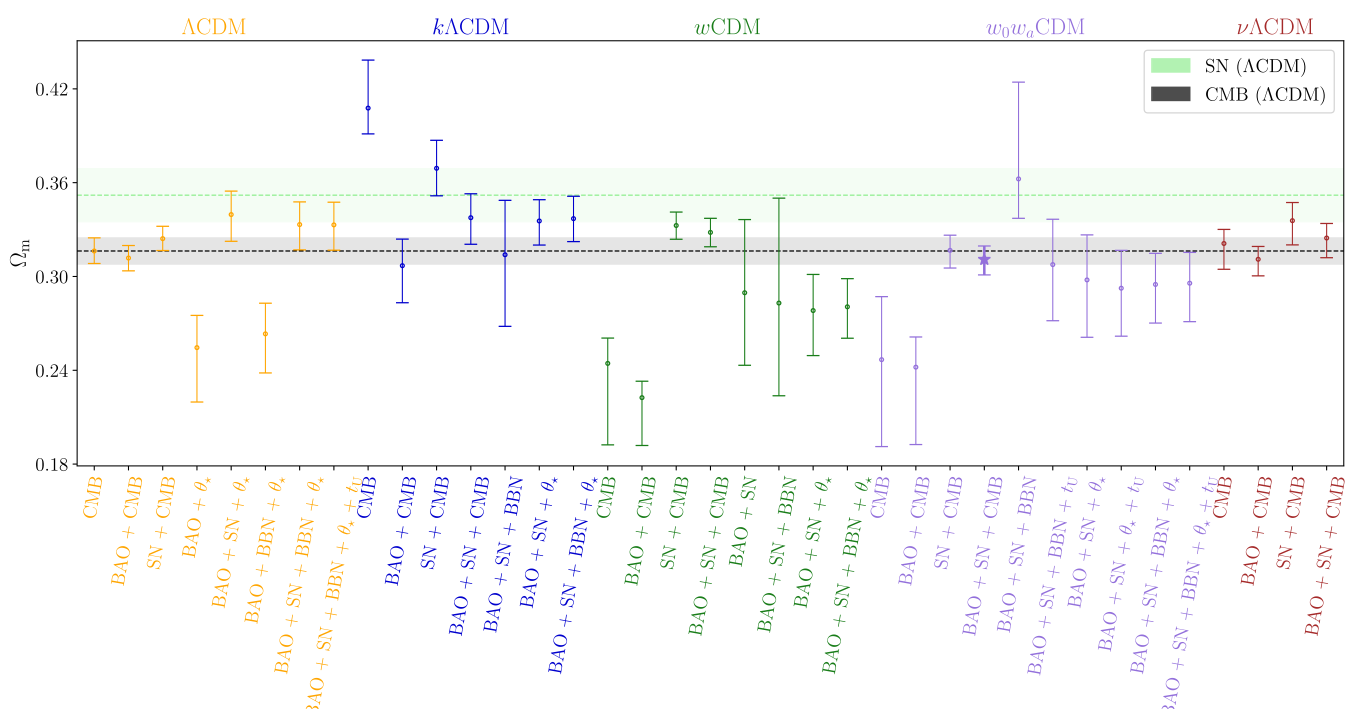

FIG. 9. Density parameter of matter in the Universe, $\Omega_{\rm m}$, with its corresponding 68% c.r. (points with error bars) or 95% upper/lower limit (triangles pointed down/up), given by the constraints for different combinations of models and datasets considered in this work. We also show the CMB-ΛCDM and SN-ΛCDM constraints, noting their full posterior are 1.7σ apart (Table IV, Sec. III C 2). Note that $\Omega_{\rm m}$ anticorrelates with H_0 (shown in Fig. 8) when including CMB and other probe combinations. Some of the more extreme constraints can be related to tensions between datasets, as is discussed in Sec. IV G. Our main results, BAO + SN + CMB w_0w_aCDM, are marked with a star.

is in tension with SN at 2.5σ. The BAO + CMB combination barely constrains H_0 in w_0w_aCDM.
(v) SN pushes to lower values of H_0 (via the Ω_m-H_0 degeneracy) when added to CMB in all the extensions.
(vi) CMB constraints on H_0 significantly relax when extending the model beyond ΛCDM. However, combining the CMB with both SN and BAO recovers tight constraints on H_0. These combinations are always compatible with the H_0 value inferred for CMB-ΛCDM.
(vii) The cosmographic expansion (Sec. IV F) BAO + SN + r_d gives $H_0 = 68.6^{+1.7}_{-1.6}\ \mathrm{km\,s^{-1}\,Mpc^{-1}}$, compatible with CMB-ΛCDM, and is robust against the order considered in the expansion.
(viii) Remarkably, in w_0w_aCDM where all the tensions among datasets disappear, we find a very tight constraint from BAO + SN + CMB, despite the flexibility of the model, $H_0 = 67.81^{+0.96}_{-0.86}\ \mathrm{km\,s^{-1}\,Mpc^{-1}}$.
(ix) In w_0w_aCDM, when using only expansion history probes (BAO + SN + BBN + $\theta_\star$ + t_U), we obtain again a well-constrained Hubble constant, $H_0 = 67.8^{+1.1}_{-1.2}\ \mathrm{km\,s^{-1}\,Mpc^{-1}}$.

Hence, we conclude that the tensions seen in ΛCDM, kΛCDM, and wCDM among probes do not seem to hint at a resolution of the Hubble tension problem, and our data combinations tend to favor H_0 values similar to ΛCDM CMB constraints.

V. DISCUSSION

A. Findings and tensions in ΛCDM and one-parameter extensions

A recurring theme of this work is that in most of the cosmological models we consider, we find some level of tension between datasets, often with our two background probes, BAO and SN, pulling in different directions of parameter space. With this in mind, we summarize the main findings for ΛCDM and its one-parameter extensions:

(1) ΛCDM
  (a) When adding BAO to CMB, it pushes for lower values of Ω_m, whereas SN pushes in the opposite direction. This is consistently found in other cosmological models.
  (b) Several tensions among data and/or inconsistencies are found. For example, BAO + BBN + $\theta_\star$ is found in 2.9σ tension with SN.
  (c) The age-of-the-Universe priors can help alleviate some tensions.
  (d) The combination BAO + SN + BBN + $\theta_\star$ can set competitive results to CMB, and are within $\sim 1\sigma$ of it.

(2) kΛCDM
  (a) CMB alone is subject to significant geometric degeneracies and prefers negative Ω_k. When adding BAO, it becomes compatible with $\Omega_k = 0$, whereas SN tightens the constraints around negative values of Ω_k. The combination BAO + SN + CMB is within $\sim 1\sigma$ of flatness.
  (b) BAO + SN + BBN + $\theta_\star$, with 2.8σ evidence for positive Ω_k, is not compatible with CMB and its combination with SN and/or BAO.
  (c) BAO is found to be in 3.2σ tension with CMB in this model.
  (d) Considering BAO + SN + CMB, the detection of dark energy is at $\sim 40\sigma$.[14]

(3) wCDM
  (a) CMB alone has a very large degeneracy between w and Ω_m, preferring $w < -1$ at 1.7σ. When adding BAO, contours tighten, preferring $w < -1$ at 2.8σ. On the other hand, SN prefers $w > -1$ ($w = -0.82^{+0.15}_{-0.11}$), remaining nearly identical if we also add BAO.
  (b) This difference in the preferred value of w leads to a tension of $\sim 2.5\sigma$ between BAO + CMB and SN in wCDM. This can be interpreted as mild hint for evolving dark energy, given that the effective redshifts of SN and BAO are different.
  (c) The combination of BAO + SN + CMB gives a preference for an accelerating fluid ($w < -1/3$) at a significance of $\sim 20\sigma$[14].

(4) νΛCDM
  (a) In this model, tensions among probes remain at a similar level as in ΛCDM (Table IV).
  (b) CMB alone sets $\sum m_\nu < 0.28$ eV, with a positive correlation between Ω_m and $\sum m_\nu$. Hence, the preference for higher Ω_m of SN results in a more relaxed neutrino constraint ($\sum m_\nu < 0.38$ eV) and the preference for lower Ω_m of BAO for more stringent constraint ($\sum m_\nu < 0.15$ eV). BAO + SN + CMB results are very similar to CMB alone: $\sum m_\nu < 0.27$ eV.

We find it difficult to reconcile all the data with these models and report our main results within w_0w_aCDM, where tensions are alleviated and different data combinations agree. We argue this choice below and present the main w_0w_aCDM conclusions in Sec. VI.

B. Is w_0w_aCDM preferred over ΛCDM ?

Our choice of w_0w_aCDM model for the main results is driven by the tensions between inferences from different datasets observed in the other models: all have at least one case of $\geq 2.5\sigma$ tension (Table IV).[15] In addition to tensions explicitly reported in Table IV and mathematically defined in Sec. III C 2, there are additional significant offsets in the

[14] Unlike the rest of the paper, here we simply divide by the σ to estimate these tensions.

[15] Additionally, recent works like [88] suggest that tensions in Ω_m in ΛCDM would naturally appear if the Universe followed a w_0w_aCDM cosmology.

posteriors inferred for different data combinations shown in Figs. 2, 4, and 5. These latter tensions cannot be quantified by the methodology in Sec. III C 2 when part of the data is shared among the two data combinations considered. Both types of tensions get significantly relieved in w_0w_aCDM, with a maximum tension of only 1.6σ among seven data combinations tested. Furthermore, all data combinations tested have 1-σ regions that overlap in the w_0-w_a plane, and several of them report $>2\sigma$ deviations—mathematically defined in Sec. III C 1—from ΛCDM. For our main data combination, BAO + SN + CMB, the deviation from ΛCDM reaches the level of 3.2σ, further supporting the choice of w_0w_aCDM (Table II). We note that this is tentative evidence (p value of 0.0014), and that 5σ ($p \sim 6 \times 10^{-7}$) is typically required to claim a discovery. Nevertheless, when datasets show $\gtrsim 2\sigma$ tensions, the parameter estimates resulting from their combination are not very reliable. Hence, we show the main results in terms of w_0w_aCDM, where important tensions go away.

Some other works have relied on Bayesian evidence or some approximation to it to choose a preferred model. However, we argue here that these methods can strongly dilute their evidence as the priors widen, whereas the parameter difference method we employ (Sec. III C 1) is independent of that effect, provided the data are sufficiently constraining [and we consider it to be the case for Eqs. (25) and (27)]. We note that both methods penalize adding more free parameters (as we do in w_0w_aCDM) to compensate for the additional degrees of freedom. This penalization is explicit in the Bayesian evidence ratios. For our method, it naturally appears since given a change in goodness of fit, the significance of the deviation dilutes when having more degrees of freedom. We also see in Table III that w_0w_aCDM improves the goodness of fit by $\Delta\chi^2 \sim 12$ with respect to ΛCDM for the two most constraining data combinations. Under the Gaussian approximation for the likelihood (Wilks' theorem [76]), this corresponds to a $\sim 3\sigma$ preference for w_0w_aCDM, given the two additional degrees of freedom, in line with our method considering the full shape of the posterior in the w_0-w_a plane ($\sim 3\sigma$, Table II).

One could potentially be concerned about projection effects when extending the parameter space, or about the effect of informative priors. This effect can be present in some instances with weak constraints such as CMB alone in Fig. 6. However, probe combinations with strong constraining power such as BAO + SN + CMB or BAO + SN + BBN + $\theta_\star$ are not expected to be affected by this. To verify the robustness of constraints and the significance of their deviation from ΛCDM, we ran a series of checks on the w_0w_aCDM inferences reported in the text above for BAO + SN + CMB [Eq. (25)], BAO + SN + BBN + t_{U} [Eq. (26)] and BAO + SN + BBN + $\theta_\star$ + t_{U} [Eq. (27)]. These checks, which included the comparison of 2D marginalized posteriors with the position of the 10 highest-posterior samples from the chain, and with an approximate profile likelihood, support the idea that these constraints are not significantly impacted by projection effects. As validation of the reported parameter-shift deviation from ΛCDM, we confirmed that the isodensity contour going through the ΛCDM point in parameter space is well behaved—i.e., that it is not dominated by noise.

Hence, we conclude that among the models tested in this paper, w_0w_aCDM is the only one capable of reconciling all the data without $\sim 2.5\sigma$ tensions, and preferred over ΛCDM at a significance of $\sim 3\sigma$. Whereas other models of the expansion history might offer another solution, exploring more alternative models is beyond the scope of this paper. Another possibility would be that one or several datasets have unaccounted for systematic errors. Both the Y6 BAO paper series [6,7] and the DES-SN5YR paper series [8,44] have already scrutinized and quantified a large ensemble of known systematic errors, which are subdominant and added in quadrature to the statistical error. Hence, all the known systematics are already accounted for, although it is always possible that a source of unknown systematics is present. Nevertheless, none of the tests point in the direction of having to exclude one particular dataset. Furthermore, reanalyzing their systematic errors, which were thoroughly analyzed in previous studies, is not the goal of this paper.

C. The Hubble constant

Given the choice of w_0w_aCDM results as our main focus, we can consider the implications for the Hubble tension, referring to H_0 constraints examined in Sec. IV G. We report a consensus value given by BAO + SN + CMB w_0w_aCDM of

$$H_0 = 67.81^{+0.96}_{-0.86}\ \mathrm{km\,s^{-1}\,Mpc^{-1}},$$

noting that this value is in good agreement with that given by CMB-ΛCDM ($H_0 = 67.30^{+0.57}_{-0.61}$ $\mathrm{km\,s^{-1}\,Mpc^{-1}}$) and BAO+SN+CMB-ΛCDM ($H_0 = 67.03^{+0.53}_{-0.55}$ $\mathrm{km\,s^{-1}\,Mpc^{-1}}$). It is also compatible with BAO + SN + CMB constraints in all models considered, as well as with the cosmographic expansion model (BAO + SN + r_d at fourth order, $H_0 = 68.6^{+1.7}_{-1.6}$ $\mathrm{km\,s^{-1}\,Mpc^{-1}}$; see Sec. IV F). This inference is also consistent with the CMB-independent data combination BAO + SN + BBN + t_{U} ($H_0 = 69.6^{+2.4}_{-2.5}$ $\mathrm{km\,s^{-1}\,Mpc^{-1}}$ in w_0w_aCDM) and with the background-probe combination BAO+SN+BBN+$\theta_\star$+t_{U} ($H_0 = 67.8^{+1.1}_{-1.2}$ $\mathrm{km\,s^{-1}\,Mpc^{-1}}$ in w_0w_aCDM). Whereas we find some higher or lower values of H_0 for certain other combinations of datasets and models, these values are always associated with tensions seen between probes. In summary, the inferred value of H_0 from the data we consider is fairly robust to different choices for model and data combinations, and the improved fit for w_0w_aCDM does not substantially impact considerations for the Hubble tension.

VI. CONCLUSIONS

In this paper, we studied the cosmological parameter implications of background probes, BAO and SN, from the DES final dataset. We did this in combination with external probes: *Planck* 's CMB (in three different forms: temperature and polarization power spectra, angular acoustic scale, $\theta_\star$, or comoving acoustic scale, r_d), BBN [60], and age-of-the-Universe priors [56], as explained in Sec. II. We studied the ΛCDM model, extensions on the background evolution (kΛCDM, wCDM, and w_0w_aCDM, see Sec. III A), and an extension with free neutrino masses (νΛCDM).

Following from the discussion above, our main conclusion is that these datasets fail to agree in parameter space at the $\gtrsim 2.5\sigma$ level (Sec. III C) except for the most complex model we considered here, w_0w_aCDM, where datasets are consistent (see Sec. V for the discussion on findings in ΛCDM, wCDM, kΛCDM, and νΛCDM, as well as why we choose to express our main conclusions in terms of w_0w_aCDM). This corresponds to the model known as CPL, where the equation of state of dark energy varies linearly with the scale factor $[w(a) = w_0 + (1-a)w_a]$. In this parameter space, our data combination of BAO + SN + CMB prefers $\{w_0 > -1, w_a < 0\}$ [Eq. (25)] over ΛCDM ($\{w_0 = -1, w_a = 0\}$) with a significance of $\sim 3.2\sigma$ (always, as defined in Sec. III C 1),

$$\left.\begin{aligned} w_0 &= -0.673^{+0.098}_{-0.097} \\ w_a &= -1.37^{+0.51}_{-0.50} \end{aligned}\right\} \mathrm{BAO} + \mathrm{SN} + \mathrm{CMB}.$$

Within the w_0w_aCDM model, all datasets considered are compatible with one another and the consensus lies in the $\{w_0 > -1, w_a < 0\}$ quadrant. This result is partly driven by SN preferring $w_0 > -1$ and BAO pushing for $w_a < 0$. We also highlight the cases where we restrict ourselves to only background probes ($\mathrm{BAO} + \mathrm{SN} + \mathrm{BBN} + \theta_\star + t_\mathrm{U}$) or non-CMB ($\mathrm{BAO} + \mathrm{SN} + \mathrm{BBN} + t_\mathrm{U}$). While these constraints are looser, they are compatible with the above combination in the $\{w_0 - wa\}$ plane and find a milder deviation of 2.8σ and 2.0σ, respectively, from ΛCDM in that plane (see Sec. III C 1).

These results could indeed be hinting at the dynamical nature of dark energy, or they could be a sign of some unknown systematic error in some (parts of the) datasets or of another type of non-ΛCDM physics shaping the expansion history of the Universe.

Certainly, this and recent works create an interesting scenario for our understanding of the cosmological model. Whereas in the recent past, the description of dark energy dynamics in ΛCDM has been in reasonably good agreement with nearly all observables studied, this has shifted in the last year. First, the final DES-SN5YR results released in January 2024 [8] reported a $\sim 2\sigma$ hint of deviation from ΛCDM in favor of the w_0w_aCDM model. Shortly after, DES-Y6-BAO found another 2.1σ hint of deviation between its measurement of $D_M(z = 0.85)/r_d$ and that predicted by *Planck* -ΛCDM [6] (although we note a similar level of deviation was previously observed in DES-Y3-BAO [26]). Finally, in April of the same year, DESI reported a 3.9σ deviation from ΛCDM when combining DESI 2024 BAO with *Planck* -CMB and DES-SN5YR SN. Reanalyzing that same data, we reproduce this result (Appendix A), finding a 3.6σ tension when using our model comparison methodology (Sec. III C), and CMB likelihood configuration (which, as we note in Sec. II C is slightly different than that used in the DESI paper).

This work confirms that the previously observed tension persists at a similar level (3.2σ) when considering DES Y6 BAO combined with DES-SN5YR and *Planck* -CMB. For comparison, we note that substituting the single DES (angular) BAO data point for the seven DESI BAO measurements [22] in combination with the same SN and CMB likelihoods only slightly increases the significance of the reported deviation from ΛCDM from 3.2σ to 3.6σ. We also find that the deviation from ΛCDM becomes larger when including both DESI and DES BAO, though the exact significance would depend on the unknown (but likely small) correlations between these datasets.

Overall, this work adds to the growing evidence from different studies that the equation of state of dark energy could vary with time. However, before a change of paradigm of this magnitude can be established, the community should require a larger statistical significance (canonically, 5σ), and this tension should persist over several years with new datasets or new probes and careful scrutiny of data characterization and analysis methodology. Our datasets include in their uncertainties a contribution from all known systematic errors, which are in all cases smaller than the statistical one. However, it is always possible that unknown systematic errors are present, and new validations should be pursued.[16] Additionally, a physical model of cosmic acceleration that is more well motivated from first principles would help establish a viable alternative to ΛCDM.

This study represents the impact of DES background cosmology probes (BAO and SN) on the current cosmological paradigm from the survey's final dataset. Looking ahead, DES will soon be releasing analyses that additionally probe the growth of structure and the density perturbations in the late-time Universe. These include studies of weak gravitational lensing, galaxy clustering, cluster counts, cross-correlations among those probes and also with external datasets, such as the CMB. These upcoming results will both provide better constraints on the properties

[16]In these lines, an alternative cross-calibration between DES and external SN appeared during the review of this paper [89]. The impact of the recalibration in the SN + BAO + CMB will be evaluated in [90], together with the impact of the new DESI DR2 BAO data.

of our cosmological models and provide crucial cross-checks of whether the emerging paradigm shift is self-consistent across probes. Certainly, the legacy of DES will be a rich source of insight for state-of-the-art cosmological analyses in the coming years.

ACKNOWLEDGMENTS

Funding for the DES Projects has been provided by the U.S. Department of Energy, the U.S. National Science Foundation, the Ministry of Science and Education of Spain, the Science and Technology Facilities Council of the United Kingdom, the Higher Education Funding Council for England, the National Center for Supercomputing Applications at the University of Illinois at Urbana-Champaign, the Kavli Institute of Cosmological Physics at the University of Chicago, the Center for Cosmology and Astro-Particle Physics at the Ohio State University, the Mitchell Institute for Fundamental Physics and Astronomy at Texas A&M University, Financiadora de Estudos e Projetos, Fundação Carlos Chagas Filho de Amparo à Pesquisa do Estado do Rio de Janeiro, Conselho Nacional de Desenvolvimento Científico e Tecnológico and the Ministério da Ciência, Tecnologia e Inovação, the Deutsche Forschungsgemeinschaft and the Collaborating Institutions in the Dark Energy Survey. The Collaborating Institutions are Argonne National Laboratory, the University of California at Santa Cruz, the University of Cambridge, Centro de Investigaciones Energéticas, Medioambientales y Tecnológicas-Madrid, the University of Chicago, University College London, the DES-Brazil Consortium, the University of Edinburgh, the Eidgenössische Technische Hochschule (ETH) Zürich, Fermi National Accelerator Laboratory, the University of Illinois at Urbana-Champaign, the Institut de Ciències de l'Espai (IEEC/CSIC), the Institut de Física d'Altes Energies, Lawrence Berkeley National Laboratory, the Ludwig-Maximilians Universität München and the associated Excellence Cluster Universe, the University of Michigan, NSF NOIRLab, the University of Nottingham, The Ohio State University, the University of Pennsylvania, the University of Portsmouth, SLAC National Accelerator Laboratory, Stanford University, the University of Sussex, Texas A&M University, and the OzDES Membership Consortium. Based in part on observations at NSF Cerro Tololo Inter-American Observatory at NSF NOIRLab (NOIRLab Prop. ID 2012B-0001; PI: J. Frieman), which is managed by the Association of Universities for Research in Astronomy (AURA) under a cooperative agreement with the National Science Foundation. The DES data management system is supported by the National Science Foundation under Grants No. AST-1138766 and No. AST-1536171. The DES participants from Spanish institutions are partially supported by MICINN under Grants No. PID2021-123012, No. PID2021-128989, No. PID2022-141079, No. PID2023-151307NB-I00, No. SEV-2016-0588, No. CEX2020-001058-M, and No. CEX2020-001007-S, some of which include ERDF funds from the European Union. I. F. A. E. is partially funded by the CERCA program of the Generalitat de Catalunya. We acknowledge support from the Brazilian Instituto Nacional de Ciência e Tecnologia (INCT) do e-Universo (CNPq Grant No. 465376/2014-2). This document was prepared by the DES Collaboration using the resources of the Fermi National Accelerator Laboratory (Fermilab), a U.S. Department of Energy, Office of Science, Office of High Energy Physics HEP User Facility. Fermilab is managed by Fermi Forward Discovery Group, LLC, acting under Contract No. 89243024CSC000002. This work used computing resources from the Duke Compute Cluster, NERSC, the Sciama cluster in Portsmouth, and Symmetry at Perimeter Institute. The DESSN Hubble diagram and analysis pipeline was made possible by the codebases `SNANA` [91] and `PIPPIN` [92]. Some of the computing for this project was performed on the Sherlock cluster. We would like to thank Stanford University and the Stanford Research Computing Center for providing computational resources and support that contributed to these research results. This research was supported in part by Perimeter Institute for Theoretical Physics. Research at Perimeter Institute is supported by the Government of Canada through the Department of Innovation, Science, and Economic Development, and by the Province of Ontario through the Ministry of Colleges and Universities. S. A. acknowledges support from the RYC2022-037311-I fellowship funded by MCIN/AEI/10.13039/501100011033 (Spain) and FSE+ (Europe). JMu thanks discussions with Z. Weiner. APo acknowledges support from the EU's Horizon Europe program under the MSCA Grant Agreement No. 101068581 and the "César Nombela" Research Talent Attraction Aid from the Community of Madrid (2023-T1/TEC29011).

All authors contributed to this paper and/or carried out infrastructure work that made this analysis possible. Some highlighted contributions from the authors of this paper include: *Scientific management and coordination:* S. Avila, A. Porredon, M. Vincenzi (science working group conveners of Large-Scale Structure, Supernova). *Significant contributions to project development, including paper writing and figures:* S. Avila, T. Davis, J. Mena-Fernández, J. Muir, A. Porredon, P. Shah, M. Vincenzi. *Data analysis, scientific interpretation, code development*: R. Camilleri, G. Campailla, N. Deiosso, A. Ferté, J. Mena-Fernández, J. Muir, M. Raveri, P. Shah. *Internal reviewing of the paper*: D. Huterer, S. Lee, P. Wiseman. *Contribution to the BAO results/catalog:* S. Avila, H. Camacho, R. Cawthon, K. C. Chan, J. De Vicente, J. Elvin-Poole, I. Ferrero, G. Giannini. J. Mena-Fernández, A. Porredon, M. Rodriguez-Monroy, I. Sevilla-Noarbe, L. Toribio San

Cipriano, E. Sanchez and N. Weaverdyck. *Construction and validation of the DES-SN5YR Hubble diagram:* P. Armstrong, D. Brout, A. Carr, R. Chen, T. M. Davis, L. Galbany, S. Hinton, R. Kessler, J. Lee, C. Lidman, A. Möller, B. Popovic, H. Qu, M. Sako, B. Sanchez, D. Scolnic, M. Smith, M. Sullivan, G. Taylor, M. Toy, P. Wiseman. *Construction and validation of the DES Gold catalog*: M. Adamow, K. Bechtol, A. Carnero Rosell, H. T. Diehl, A. Drlica-Wagner, R. A. Gruendl, W. G. Hartley, A. Pieres, E. S. Rykoff, I. Sevilla-Noarbe, E. Sheldon, and B. Yanny. The remaining authors have made contributions to this paper that include, but are not limited to, the construction of DECam and other aspects of collecting the data; data processing and calibration; developing broadly used methods, codes, and simulations; running the pipelines and validation tests; and promoting the science analysis.

DATA AVAILABILITY

The data that support the findings of this article are openly available [93], embargo periods may apply.

APPENDIX A: COMBINATION WITH DESI 2024 BAO

In this appendix, we combine our BAO and SN measurements with the DESI 2024 BAO results from [21], and also CMB from *Planck*, and run chains assuming $w_0 w_a$CDM. We include all BAO measurements from DESI, namely BGS, LRG1, LRG2, LRG3 + ELG1, ELG2, QSO, and LYA. In Fig. 10, we show the angular BAO distance ladder, including the results from DESI 2024 and our DES BAO measurement. For BGS and QSO, the 2D BAO fit was not carried out; therefore, there is no D_M/r_d available in the table mentioned above. For these two tracers, we plot D_V/r_d as the value for D_M/r_d represented in the plot and $1.5 \times \sigma(D_V/r_d)$ as its uncertainty.[17] Nevertheless, for the chains, the full likelihood of DESI 2024 BAO is used, considering D_M/r_d and D_H/r_d when available, and D_V/r_d when not. This is labeled as DESI2024BAO.

The results of our chains are shown in Fig. 11. The CMB + DESI2024BAO combination (blue) is 2.8σ away from ΛCDM (see Table VI), compared to the 3.4σ deviation found with BAO + CMB (Table II). When adding SN (SN + CMB + DESI2024BAO, red), the deviation rises to 3.6σ (Table VI), compared to the 3.2σ we found with DES BAO in combination with CMB and SN (Table II). Nevertheless, we see that DESI alone does not show a strong deviation from ΛCDM.

[17]Assuming spherical symmetry, the $D_M(z)$ constraints are 50% less precise (see [94]) with respect to the spherically averaged measurement.

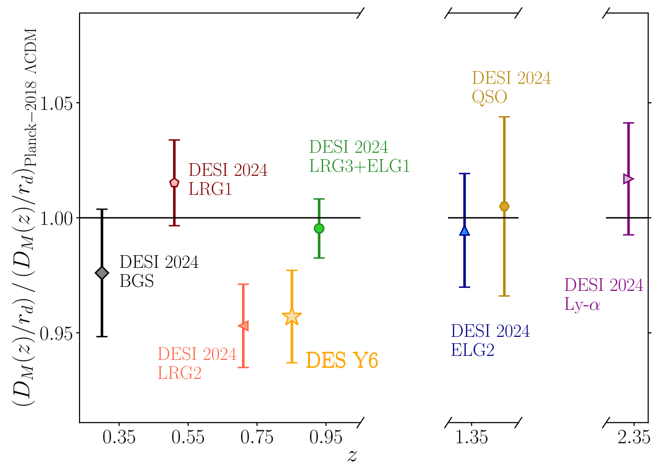

FIG. 10. Ratio between the $D_M(z)/r_d$ measured using the BAO feature at different redshifts and the prediction from the cosmological parameters determined by *Planck* -2018, assuming ΛCDM. We include all the measurements from the DESI 2024 BAO analysis in different colors, and the DES Y6 measurement as an golden star.

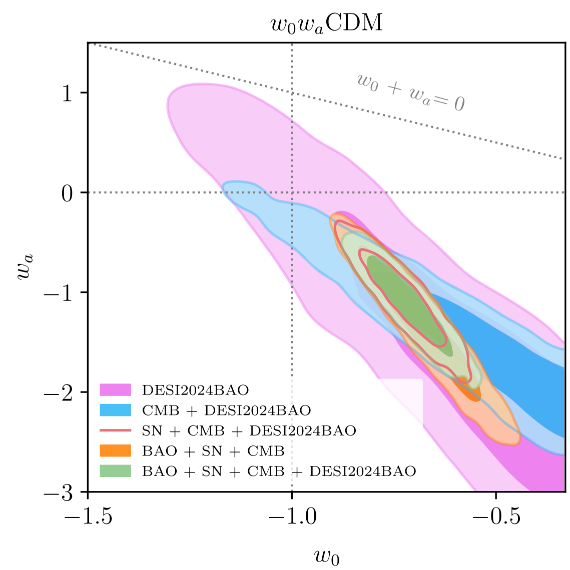

FIG. 11. $w_0 w_a$CDM with DESI. 1 and 2σ contours of the 2D posterior of w_0-w_a for several data combinations that include DESI 2024 BAO, labeled as DESI2024BAO. We also include combinations with DES BAO (simply labeled as BAO), in particular, the orange BAO + SN + CMB contour is the same one as in Fig. 6. Combining CMB, SN, and either BAO dataset (DES or DESI), the deviation from ΛCDM is $> 3\sigma$. The deviation could be larger for the green case with both BAO datasets combined; however, possible correlations among them have been neglected in this combination, see discussion in Appendix A.

We also note that the 3.6σ deviation found here for SN + CMB + DESI2024BAO is somewhat lower than that reported by DESI (3.9σ [22]). This is due to two main reasons. First, the CMB implementation is somewhat different (see Sec. II C), mainly because we do not include

TABLE VI. Deviations from ΛCDM of the constraints in the w_0w_aCDM model for data combinations that include DESI 2024 BAO results; see Appendix A. This is quantified in σs, see Eq. (21) and Sec. III C 1. We note that possible correlations between DESI BAO and DES BAO (simply labeled as BAO) are neglected and could reduce the deviation reported in the last row.

	Deviations from ΛCDM (σ)
Dataset	w_0w_aCDM
DESI2024BAO	1.3
CMB + DESI2024BAO	2.8
SN + CMB + DESI2024BAO	3.6
BAO + SN + CMB + DESI2024BAO	4.2

CMB-lensing in our likelihood, but [22] did. Second, DESI used likelihood ratios to estimate the deviation based on $\Delta\chi^2$ and Wilks' theorem, while we consider the full shape of the posterior in the w_0-w_a parameter plane as our primary metric; see Sec. III C 1. If we use the same likelihood ratio method as DESI, we find a deviation of 4.0σ from $\Delta\chi^2 = 18.9$.

Finally, we also report the combination of CMB, SN together with both BAO datasets (BAO + SN + CMB + DESI2024BAO, green in Fig. 11). In this case, the parameter shift deviation from ΛCDM is at the 4.2σ level while the goodness-of-fit comparison gives $\Delta\chi^2 = 18.9$ and 4.0σ. Nevertheless, we caution that this number relies on DES BAO and DESI BAO being fully independent. There is some small overlap in the area and redshift range of the samples that could give rise to some small correlations among these datasets. This correlation is expected to be small, but computing it is beyond the scope of this paper.

APPENDIX B: LIKELIHOOD FOR BAO INDIVIDUAL BINS

In [6], we presented measurements of the BAO shift α from the angular correlation function (ACF) over the entire BAO sample redshift range ($0.6 < z_{\rm ph} < 1.2$). This method was validated with 1952 mocks. Along with it, two other methods were validated: the angular power spectrum (APS) and projected correlation function.

In this appendix, we validate the method when computed at the individual bin level, with $\Delta z_{\rm ph} = 0.1$. In this process, we found ACF to be more robust than APS and PCF, so we will only continue with ACF.

The main validation is given by Table VII, similar to Table III of [6]. The method minimizes the χ^2 as a function of α, defining the best fit as the minimum χ^2 and the error

TABLE VII. Validation of the angular correlation function method on individual tomographic bins, when run in the 1952 COLA mocks. We show (i) bin number, (2) redshift interval, (3) mean of the best fit BAO shift (α) across all mocks, (4) standard deviation of best fit α, (5) semiwidth of the interval containing 68% of the best fit α, (6) mean of the error reported in each mock, and (7) number of mocks with a best fit within $[\langle\alpha\rangle - \langle\sigma_\alpha\rangle, \langle\alpha\rangle + \langle\sigma_\alpha\rangle]$. This table is the equivalent of Table III of [6] but for individual bins.

Bins	Redshift	$\langle\alpha\rangle$	$\sigma_{\rm std}$	σ_{68}	$\langle\sigma_\alpha\rangle$	Mocks $\in \langle\alpha\rangle \pm \langle\sigma_\alpha\rangle$
1	$0.6 < z_{\rm ph} < 0.7$	1.0024	0.0485	0.0457	0.0454	67.7%
2	$0.7 < z_{\rm ph} < 0.8$	0.9999	0.0458	0.0438	0.0420	66.2%
3	$0.8 < z_{\rm ph} < 0.9$	1.0038	0.0407	0.0388	0.0403	70.0%
4	$0.9 < z_{\rm ph} < 1.0$	1.0095	0.0398	0.0370	0.0376	69.2%
5	$1.0 < z_{\rm ph} < 1.1$	1.0072	0.0409	0.0377	0.0416	72.4%
6	$1.1 < z_{\rm ph} < 1.2$	1.0067	0.0475	0.0461	0.0557	76.0%

TABLE VIII. DES BAO fits. The second column ($0.6 < z_{\rm ph} < 1.2$) point shows the main results from [6] using the entire BAO sample and the combination of the three clustering estimators: ACF, APS, and PCF. The next six columns consider the individual data using only the ACF. The first bin ($0.6 < z_{\rm ph} < 0.7$) does not have a detection according to our criteria. In the first row, we show the best fit BAO shift (α) with its associated statistical error bar, we then report two sources of systematic errors (from redshift calibration and modeling) and finally, the total error bar ($\sigma_{\rm tot}$) summing in quadrature the three. In the last tier, we also report the effective redshift [$z_{\rm eff}$, Eq. (25) of [6] and the final physical constraints in terms of $D_M(z_{\rm eff})/r_d$] that goes into the likelihood.

Bin	$0.6<z_{\rm ph}<1.2$	$0.6<z_{\rm ph}<0.7$	$0.7<z_{\rm ph}<0.8$	$0.8<z_{\rm ph}<0.9$	$0.9<z_{\rm ph}<1.0$	$1.0<z_{\rm ph}<1.1$	$1.1<z_{\rm ph}<1.2$
$\alpha\pm\sigma_{\rm stat}$	0.9571 ± 0.0196	⋯	0.9279 ± 0.0404	0.9649 ± 0.0434	0.9974 ± 0.0557	0.9511 ± 0.0551	1.0515 ± 0.0775
$\sigma_{z,{\rm sys}}$	⋯	0.0151	0.0079	0.0082	0.0112	0.0030	0.0062
$\sigma_{\rm mod,sys}$	⋯	0.0024	0.0001	0.0038	0.0095	0.0072	0.0067
$\alpha\pm\sigma_{\rm tot}$	⋯	⋯	0.9279 ± 0.0412	0.9649 ± 0.0443	0.9974 ± 0.0576	0.9511 ± 0.0556	1.0515 ± 0.0780
$z_{\rm eff}$	0.851	0.652	0.752	0.850	0.947	1.043	1.142
D_M/r_d	19.51 ± 0.41	⋯	17.18 ± 0.75	19.66 ± 0.88	22.05 ± 1.23	22.57 ± 1.31	26.62 ± 1.96

σ_α as the semiwidth of the $\Delta\chi^2 = 1$ region. In Table VII, we find the mean of the best fits, $\langle\alpha\rangle$, which is expected to be 1, since in the mocks we assume the cosmology they were generated with. We then use $|\langle\alpha\rangle - 1|$ as a systematic error associated to modeling in each individual bin, which we report in Table VIII as $\sigma_{\rm mod,sys}$. We also check the reasonable agreement between $\langle\sigma_\alpha\rangle$, $\sigma_{\rm std}$ and σ_{68}, which tells us about the robustness of our error bars. We refer the reader to [6] for more details.

In Table VIII, we report our measurements of the individual bin BAO. The systematic error associated to modeling ($\sigma_{z,\rm mod}$) comes from Table VII described in the previous paragraph. The systematic error associated with redshifts ($\sigma_{z,\rm sys}$) comes from Table I of [6]. The total error is computed as the sum of the quadrature of those two with the statistical error. This is the same procedure we followed in [6] for the combined measurement ($0.6 < z_{\rm ph} < 1.2$). Then, multiplying α by the fiducial D_M/r_d from the cosmology assumed in the template fitted to the data, we obtain physical constraints on D_M/r_d.

Finally, we note that these individual measurements are expected to be correlated, mostly due to their redshift overlap (Fig. 2 of [6]). Using the 1952 mock catalogues we compute the Pearson correlation coefficient (ρ_{ij}) among any two bins (i, j) and represent them in Fig. 12. Then, our final covariance comes from the total error (σ) reported on the last row of Table VIII and the correlation from Fig. 12,

$$C_{i,j} = \sigma_i \sigma_j \rho_{ij}. \tag{B1}$$

With this covariance, and the mean of $\bar{D} \equiv D_M/r_d$ reported in Table VIII, we construct a Gaussian likelihood $[\log\mathcal{L} \propto (D_i(\mathbf{p}) - \bar{D}_i) C^{-1}_{i,j} (D_j(\mathbf{p}) - \bar{D}_j)]$.

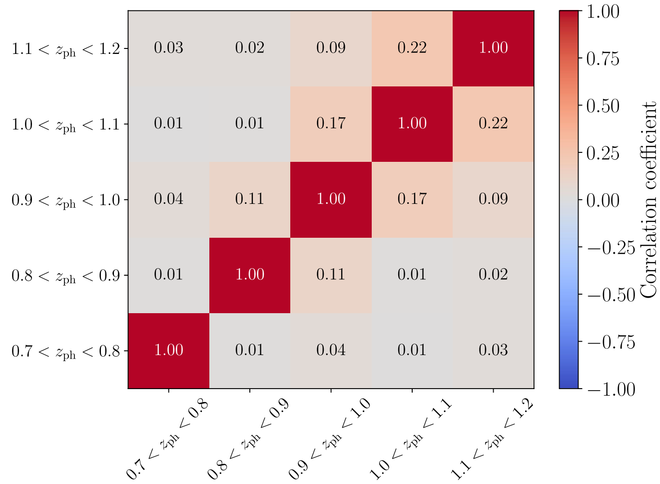

FIG. 12. Correlation matrix of α_i for the five redshift bins with an individual BAO detection.

APPENDIX C: COSMOLOGICAL CONSTRAINTS FROM THE BAO INDIVIDUAL BINS

Once we have set up the alternative individual bin likelihood in Appendix B, we can rerun our chains. We will simply focus on BAO + CMB, where the impact of BAO is expected to be more notable. Even in this case, in Fig. 13, we barely see any difference with respect to the standard BAO likelihood. In other cases that were explored, but not shown, we also found a negligible effect of swapping the BAO likelihoods. Hence, we conclude that the different α values preferred by different redshift bins are likely due to statistical fluctuations (note that in [6] we already found α_i redshift fluctuations consistent with that of the 1952 mocks) rather than hinting to an expansion history different to that preferred by the single BAO case.

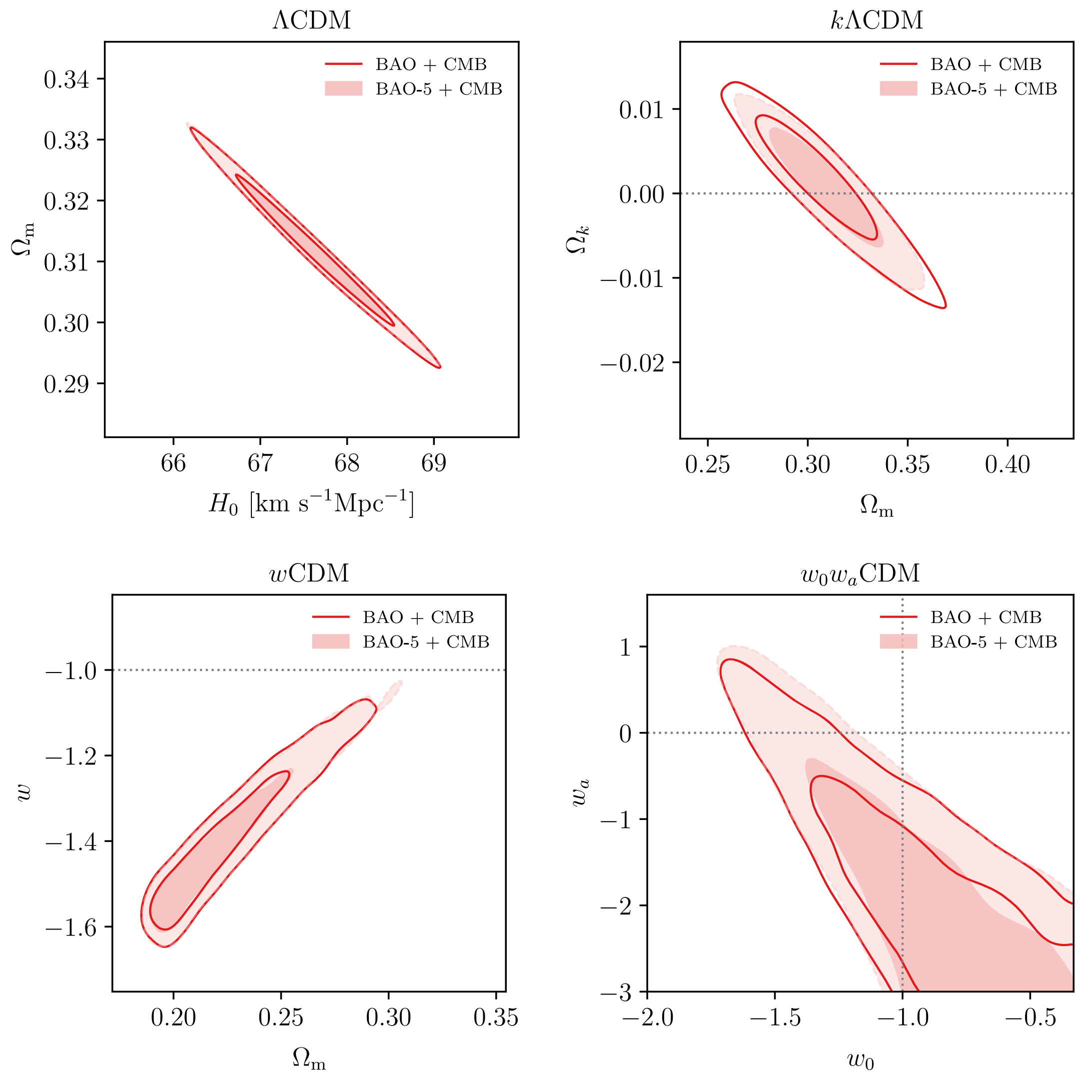

FIG. 13. Comparison of constraints from CMB in combination with the standard DES BAO constraint (BAO: 1 D_M/r_d point in $0.6 < z_{ph} < 1.2$) and the combination with the alternative BAO analysis based on five individual bins (BAO-5: D_M/r_d fitted in each of the $\Delta z_{ph} = 0.1$ bins). We show constraints in ΛCDM, kΛCDM, wCDM, and w_0w_aCDM, finding very small differences.

[1] DES Collaboration, The Dark Energy Survey, arXiv:astro-ph/0510346.

[2] DES Collaboration, The Dark Energy Survey: More than dark energy—An overview, Mon. Not. R. Astron. Soc. **460**, 1270 (2016).

[3] B. Flaugher, H. T. Diehl, K. Honscheid *et al.* (DES Collaboration), The dark energy camera, Astron. J. **150**, 150 (2015).

[4] DES Collaboration, Cosmological constraints from multiple probes in the Dark Energy Survey, Phys. Rev. Lett. **122**, 171301 (2019).

[5] DES Collaboration, The Dark Energy Survey data release 2, Astrophys. J. Suppl. Ser. **255**, 20 (2021).

[6] DES Collaboration, Dark Energy Survey: A 2.1% measurement of the angular baryonic acoustic oscillation scale at redshift $z_{eff} = 0.85$ from the final dataset, Phys. Rev. D **110**, 063515 (2024).

[7] J. Mena-Fernández *et al.* (DES Collaboration), Dark Energy Survey: Galaxy sample for the baryonic acoustic oscillation measurement from the final dataset, Phys. Rev. D **110**, 063514 (2024).

[8] DES Collaboration, The Dark Energy Survey: Cosmology results with ∼1500 new high-redshift Type Ia supernovae using the Full 5 yr data Set, Astrophys. J. Lett. **973**, L14 (2024).

[9] R. Camilleri *et al.* (DES Collaboration), The Dark Energy Survey supernova program: Investigating beyond-ΛCDM, Mon. Not. R. Astron. Soc. **533**, 2615 (2024).

[10] A. Amon *et al.* (DES Collaboration), Dark Energy Survey Year 3 results: Cosmology from cosmic shear and robustness to data calibration, Phys. Rev. D **105**, 023514 (2022).

[11] L. F. Secco, S. Samuroff *et al.* (DES Collaboration), Dark Energy Survey Year 3 results: Cosmology from cosmic shear and robustness to modeling uncertainty, Phys. Rev. D **105**, 023515 (2022).

[12] M. Rodríguez-Monroy *et al.* (DES Collaboration), Dark Energy Survey Year 3 results: Galaxy clustering and systematics treatment for lens galaxy samples, Mon. Not. R. Astron. Soc. **511**, 2665 (2022).

[13] DES Collaboration, Dark Energy Survey Year 1 results: Cosmological constraints from cluster abundances and weak lensing, Phys. Rev. D **102**, 023509 (2020).

[14] A. Porredon *et al.* (DES Collaboration), Dark Energy Survey year 3 results: Cosmological constraints from galaxy clustering and galaxy-galaxy lensing using the MagLim lens sample, Phys. Rev. D **106**, 103530 (2022).

[15] S. Pandey *et al.* (DES Collaboration), Dark Energy Survey year 3 results: Constraints on cosmological parameters and galaxy-bias models from galaxy clustering and galaxy-galaxy lensing using the redMaGiC sample, Phys. Rev. D **106**, 043520 (2022).

[16] DES Collaboration, Dark Energy Survey year 3 results: Cosmological constraints from galaxy clustering and weak lensing, Phys. Rev. D **105**, 023520 (2022).

[17] DES Collaboration, Dark Energy Survey year 3 results: Constraints on extensions to ΛCDM with weak lensing and galaxy clustering, Phys. Rev. D **107**, 083504 (2023).

[18] M. Chevallier and D. Polarski, Accelerating universes with scaling dark matter, Int. J. Mod. Phys. D **10**, 213 (2001).

[19] E. V. Linder, Exploring the expansion history of the universe, Phys. Rev. Lett. **90**, 091301 (2003).

[20] DESI Collaboration, DESI 2024 VI: Cosmological constraints from the measurements of baryon acoustic oscillations, J. Cosmol. Astropart. Phys. 02 (2025) 021.

[21] DESI Collaboration, DESI 2024 III: Baryon acoustic oscillations from Galaxies and Quasars, J. Cosmol. Astropart. Phys. 04 (2025) 012.

[22] DESI Collaboration, DESI 2024 IV: Baryon acoustic oscillations from the Lyman alpha forest, J. Cosmol. Astropart. Phys. 01 (2025) 124.

[23] DESI Collaboration, DESI 2024 VII: Cosmological constraints from the full-shape modeling of clustering measurements, J. Cosmol. Astropart. Phys. 07 (2025) 028.

[24] A. Notari, M. Redi, and A. Tesi, BAO vs. SN evidence for evolving dark energy, J. Cosmol. Astropart. Phys. 04 (2025) 048.

[25] DES Collaboration, Dark Energy Survey year 1 results: Measurement of the baryon acoustic oscillation scale in the distribution of galaxies to redshift 1, Mon. Not. R. Astron. Soc. **483**, 4866 (2019).

[26] DES Collaboration, Dark Energy Survey year 3 results: A 2.7% measurement of baryon acoustic oscillation distance scale at redshift 0.835, Phys. Rev. D **105**, 043512 (2022).

[27] J. De Vicente, E. Sánchez, and I. Sevilla-Noarbe, DNF—Galaxy photometric redshift by directional neighbourhood fitting, Mon. Not. R. Astron. Soc. **459**, 3078 (2016).

[28] R. Cawthon *et al.* (DES Collaboration), Dark Energy Survey year 3 results: Calibration of lens sample redshift distributions using fclustering redshifts with BOSS/eBOSS, Mon. Not. R. Astron. Soc. **513**, 5517 (2022).

[29] L. Guzzo *et al.* (VIPERS Collaboration), The VIMOS Public Extragalactic Redshift Survey (VIPERS). An unprecedented view of galaxies and large-scale structure at $0.5 < z < 1.2$, Astron. Astrophys. **566**, A108 (2014).

[30] Elvin-Poole *et al.* (DES Collaboration), Dark Energy Survey year 1 results: Galaxy clustering for combined probes, Phys. Rev. D **98**, 042006 (2018).

[31] M. Crocce *et al.* (DES Collaboration), Dark Energy Survey year 1 results: Galaxy sample for BAO measurement, Mon. Not. R. Astron. Soc. **482**, 2807 (2019).

[32] A. Carnero Rosell *et al.* (DES Collaboration), Dark Energy Survey year 3 results: Galaxy sample for BAO measurement, Mon. Not. R. Astron. Soc. **509**, 778 (2022).

[33] K. C. Chan *et al.* (DES Collaboration), BAO from angular clustering: Optimization and mitigation of theoretical systematics, Mon. Not. R. Astron. Soc. **480**, 3031 (2018).

[34] H. Camacho *et al.* (DES Collaboration), Dark Energy Survey year 1 results: Measurement of the galaxy angular power spectrum, Mon. Not. R. Astron. Soc. **487**, 3870 (2019).

[35] A. J. Ross *et al.* (DES Collaboration), Optimized clustering estimators for BAO measurements accounting for significant redshift uncertainty, Mon. Not. R. Astron. Soc. **472**, 4456 (2017).

[36] K. C. Chan, I. Ferrero, S. Avila, A. J. Ross, M. Crocce, and E. Gaztanaga, Clustering with general photo-z uncertainties: Application to baryon acoustic oscillations, Mon. Not. R. Astron. Soc. **511**, 3965 (2022).

[37] K. C. Chan, S. Avila, A. Carnero Rosell, I. Ferrero, J. Elvin-Poole, E. Sanchez, H. Camacho, A. Porredon, M. Crocce *et al.* (DES Collaboration), Dark Energy Survey year 3 results: Measurement of the baryon acoustic oscillations with three-dimensional clustering, Phys. Rev. D **106**, 123502 (2022).

[38] A. Izard, M. Crocce, and P. Fosalba, ICE-COLA: Towards fast and accurate synthetic galaxy catalogues optimizing a quasi-N-body method, Mon. Not. R. Astron. Soc. **459**, 2327 (2016).

[39] J. Koda, C. Blake, F. Beutler, E. Kazin, and F. Marin, Fast and accurate mock catalogue generation for low-mass galaxies, Mon. Not. R. Astron. Soc. **459**, 2118 (2016).

[40] S. Avila *et al.* (DES Collaboration), Dark Energy Survey year 1 results: Galaxy mock catalogues for BAO, Mon. Not. R. Astron. Soc. **479**, 94 (2018).

[41] I. Ferrero *et al.* (DES Collaboration), Dark Energy Survey year 3 results: Galaxy mock catalogs for BAO analysis, Astron. Astrophys. **656**, A106 (2021).

[42] A. Möller and T. de Boissière, SuperNNova: An open-source framework for Bayesian, neural network-based supernova classification, Mon. Not. R. Astron. Soc. **491**, 4277 (2020).

[43] A. Möller (DES Collaboration), The Dark Energy Survey 5-yr photometrically identified Type Ia supernovae, Mon. Not. R. Astron. Soc. **514**, 5159 (2022).

[44] M. Vincenzi *et al.* (DES Collaboration), The Dark Energy Survey supernova program: Cosmological analysis and systematic uncertainties, Astrophys. J. **975**, 86 (2024).

[45] DES Collaboration, First cosmology results using Type Ia supernovae from the dark energy survey: Constraints on

cosmological parameters, Astrophys. J. Lett. **872**, L30 (2019).
[46] D. Brout, G. Taylor, D. Scolnic, C. M. Wood, B. M. Rose, M. Vincenzi, A. Dwomoh, C. Lidman, A. Riess, N. Ali, H. Qu, and M. Dai, The Pantheon + analysis: SuperCal-fragilistic cross calibration, retrained SALT2 light-curve model, and calibration systematic uncertainty, Astrophys. J. **938**, 111 (2022).
[47] B. O. Sánchez *et al.* (DES Collaboration), The Dark Energy Survey supernova program: Light curves and 5 Yr data release, Astrophys. J. **975**, 5 (2024).
[48] G. Taylor, D. O. Jones, B. Popovic, M. Vincenzi, R. Kessler, D. Scolnic, M. Dai, W. D. Kenworthy, and J. D. R. Pierel, SALT2 versus SALT3: Updated model surfaces and their impacts on type Ia supernova cosmology, Mon. Not. R. Astron. Soc. **520**, 5209 (2023).
[49] L. Kelsey *et al.* (DES Collaboration), Concerning colour: The effect of environment on type Ia supernova colour in the dark energy survey, Mon. Not. R. Astron. Soc. **519**, 3046 (2023).
[50] P. Wiseman *et al.* (DES Collaboration), Supernova host galaxies in the dark energy survey: I. Deep coadds, photometry, and stellar masses, Mon. Not. R. Astron. Soc. **495**, 4040 (2020).
[51] Planck Collaboration, Planck 2018 results. V. CMB power spectra and likelihoods, Astron. Astrophys. **641**, A5 (2020).
[52] H. Prince and J. Dunkley, Data compression in cosmology: A compressed likelihood for Planck data, Phys. Rev. D **100**, 083502 (2019).
[53] Planck Collaboration, Planck 2018 results. VI. Cosmological parameters, Astron. Astrophys. **641**, A6 (2020).
[54] P. Lemos and A. Lewis, CMB constraints on the early universe independent of late-time cosmology, Phys. Rev. D **107**, 103505 (2023).
[55] C. B. Haselgrove and F. Hoyle, A preliminary determination of the age of type II stars, Mon. Not. R. Astron. Soc. **116**, 527 (1956).
[56] D. Valcin, J. L. Bernal, R. Jimenez, L. Verde, and B. D. Wandelt, Inferring the age of the universe with globular clusters, J. Cosmol. Astropart. Phys. 12 (2020) 002.
[57] R. Jimenez, A. Cimatti, L. Verde, M. Moresco, and B. Wandelt, The local and distant Universe: Stellar ages and H_0, J. Cosmol. Astropart. Phys. 03 (2019) 043.
[58] R. J. Cooke, M. Pettini, and C. C. Steidel, One percent determination of the primordial deuterium abundance, Astrophys. J. **855**, 102 (2018).
[59] E. Aver, D. A. Berg, A. S. Hirschauer, K. A. Olive, R. W. Pogge, N. S. J. Rogers, J. J. Salzer, and E. D. Skillman, A comprehensive chemical abundance analysis of the extremely metal poor Leoncino Dwarf galaxy (AGC 198691), Mon. Not. R. Astron. Soc. **510**, 373 (2022).
[60] N. Schöneberg, The 2024 BBN baryon abundance update, J. Cosmol. Astropart. Phys. 06 (**2024**) 006.
[61] A. G. Riess, W. Yuan, L. M. Macri, D. Scolnic, D. Brout, S. Casertano, D. O. Jones, Y. Murakami, G. S. Anand, L. Breuval, T. G. Brink, A. V. Filippenko, S. Hoffmann, S. W. Jha, W. D'arcy Kenworthy, J. Mackenty, B. E. Stahl, and W. Zheng, A comprehensive measurement of the local value of the Hubble constant with 1 km s^{-1} Mpc^{-1} uncertainty from the Hubble space telescope and the SH0ES Team, Astrophys. J. Lett. **934**, L7 (2022).
[62] L. Verde, N. Schöneberg, and H. Gil-Marín, A tale of many H_0, Annu. Rev. Astron. Astrophys. **62**, 287 (2024).
[63] M. Loverde and Z. J. Weiner, Massive neutrinos and cosmic composition, J. Cosmol. Astropart. Phys. 12 (2024) 048.
[64] W. J. Handley, M. P. Hobson, and A. N. Lasenby, POLYCHORD: Next-generation nested sampling, Mon. Not. R. Astron. Soc. **453**, 4384 (2015).
[65] J. U. Lange, NAUTILUS: Boosting Bayesian importance nested sampling with deep learning, Mon. Not. R. Astron. Soc. **525**, 3181 (2023).
[66] J. Zuntz, M. Paterno, E. Jennings, D. Rudd, A. Manzotti, S. Dodelson, S. Bridle, S. Sehrish, and J. Kowalkowski, COSMOSIS: Modular cosmological parameter estimation, Astron. Comput. **12**, 45 (2015).
[67] R. Camilleri *et al.* (DES Collaboration), The Dark Energy Survey Supernova Program: An updated measurement of the Hubble constant using the inverse distance ladder, Mon. Not. R. Astron. Soc. **537**, 1818 (2025).
[68] C. Howlett, A. Lewis, A. Hall, and A. Challinor, CMB power spectrum parameter degeneracies in the era of precision cosmology, J. Cosmol. Astropart. Phys. 04 (2012) 027.
[69] A. Lewis, A. Challinor, and A. Lasenby, Efficient computation of cosmic microwave background anisotropies in closed Friedmann-Robertson-Walker models, Astrophys. J. **538**, 473 (2000).
[70] R. Takahashi, M. Sato, T. Nishimichi, A. Taruya, and M. Oguri, Revising the HALOFIT model for the nonlinear matter power spectrum, Astrophys. J. **761**, 152 (2012).
[71] S. Bird, M. Viel, and M. G. Haehnelt, Massive neutrinos and the non-linear matter power spectrum, Mon. Not. R. Astron. Soc. **420**, 2551 (2012).
[72] A. Lewis, GETDIST: A Python package for analysing Monte Carlo samples, J. Cosmol. Astropart. Phys. 08 (2025) 025.
[73] M. Raveri and C. Doux, Non-Gaussian estimates of tensions in cosmological parameters, Phys. Rev. D **104**, 043504 (2021).
[74] M. Raveri and W. Hu, Concordance and discordance in cosmology, Phys. Rev. D **99**, 043506 (2019).
[75] P. Lemos, M. Raveri *et al.* (DES Collaboration), Assessing tension metrics with dark energy survey and Planck data, Mon. Not. R. Astron. Soc. **505**, 6179 (2021).
[76] S. S. Wilks, The large-sample distribution of the likelihood ratio for testing composite hypotheses, Ann. Math. Stat. **9**, 60 (1938).
[77] G. Efstathiou and S. Gratton, The evidence for a spatially flat Universe, Mon. Not. R. Astron. Soc. **496**, L91 (2020).
[78] W. Handley, Curvature tension: Evidence for a closed universe, Phys. Rev. D **103**, L041301 (2021).
[79] E. Di Valentino, A. Melchiorri, and J. Silk, Investigating cosmic discordance, Astrophys. J. Lett. **908**, L9 (2021).
[80] A. Glanville, C. Howlett, and T. Davis, Full-shape galaxy power spectra and the curvature tension, Mon. Not. R. Astron. Soc. **517**, 3087 (2022).
[81] S. Alam (BOSS Collaboration), The clustering of galaxies in the completed SDSS-III Baryon Oscillation Spectroscopic

Survey: Cosmological analysis of the DR12 galaxy sample, Mon. Not. R. Astron. Soc. **470**, 2617 (2017).
[82] D. Green and J. Meyers, The cosmological preference for negative neutrino mass, Phys. Rev. D **111**, 083507 (2025).
[83] M. Visser, Jerk, snap and the cosmological equation of state, Classical Quantum Gravity **21**, 2603 (2004).
[84] M.-J. Zhang, H. Li, and J.-Q. Xia, What do we know about cosmography, Eur. Phys. J. C **77**, 434 (2017).
[85] BOSS Collaboration, Cosmological implications of baryon acoustic oscillation measurements, Phys. Rev. D **92**, 123516 (2015).
[86] E. Macaulay *et al.* (DES Collaboration), First cosmological results using Type Ia supernovae from the Dark Energy Survey: Measurement of the Hubble constant, Mon. Not. R. Astron. Soc. **486**, 2184 (2019).
[87] H. Akaike, A new look at the statistical model IDENTIFICATION, IEEE Trans. Autom. Control **19**, 716 (1974).
[88] X. T. Tang, D. Brout, T. Karwal, C. Chang, V. Miranda, and M. Vincenzi, Uniting the observed dynamical dark energy preference with the discrepancies in Ω_m and H_0 across cosmological probes, Astrophys. J. Lett. **983**, L27 (2025).
[89] B. Popovic, P. Shah *et al.* (DES Collaboration), The Dark Energy Survey supernova program: A reanalysis of cosmology results and evidence for evolving dark energy with an updated Type Ia supernova calibration, arXiv:2511.07517.
[90] J. Mena-Fernández *et al.* (DES Collaboration), Dark Energy Survey: DESI-independent angular BAO measurement, arXiv:2601.14864.
[91] R. Kessler, J. P. Bernstein, D. Cinabro, B. Dilday, J. A. Frieman, S. Jha, S. Kuhlmann, G. Miknaitis, M. Sako, M. Taylor, and J. Vanderplas, SNANA: A public software package for supernova analysis, Publ. Astron. Soc. Pac. **121**, 1028 (2009).
[92] S. Hinton and D. Brout, PIPPIN: A pipeline for supernova cosmology, J. Open Source Software **5**, 2122 (2020).
[93] https://des.ncsa.illinois.edu/releases.
[94] A. J. Ross, W. J. Percival, and M. Manera, The information content of anisotropic baryon acoustic oscillation scale measurements, Mon. Not. R. Astron. Soc. **451**, 1331 (2015).